Materials Today Bio 40 (2026) 103548

Contents lists available at ScienceDirect

Materials Today Bio

journal homepage: www.journals.elsevier.com/materials-today-bio

Mimicking tumor hypoxia in a glioblastoma-on-a-chip

Gaia Corallo [a,b,c,1], Laura Sercia [a,b,d,1], Alessandro De Giorgi [a,b,c,1], Francesca Scalera [a,b], Alberto Portone [a,b], Paola Franco [e], Maria Patrizia Stoppelli [e,f], Giuseppe Gigli [a,b,g], Alessandro Polini [a,b,*,2], Francesca Gervaso [a,b,**,2]

[a] Institute of Nanotechnology, National Research Council (CNR-NANOTEC), c/o Campus Ecotekne, via Monteroni, Lecce, 73100, Italy
[b] Tecnomed Puglia – Technopole for Precision Medicine (Biotech Lecce Hub), c/o Ecotekne Campus, via Monteroni, Lecce, 73100, Italy
[c] University of Salento, Dipartimento di Matematica e Fisica E. de Giorgi, c/o Campus Ecotekne, via Monteroni, Lecce, 73100, Italy
[d] University of Salento, Dipartimento di Ingegneria dell'Innovazione, c/o Campus Ecotekne, via Monteroni, Lecce, 73100, Italy
[e] Institute of Genetics and Biophysics "A. Buzzati Traverso" (CNR-IGB), National Research Council, Naples, 80131, Italy
[f] UniCamillus-Saint Camillus International University of Health Sciences, Departmental Faculty of Medicine and Surgery, Rome, 00131, Italy
[g] University of Salento, Dipartimento di Medicina Sperimentale, c/o Campus Ecotekne, Via Monteroni, Lecce, 73100, Italy

ARTICLE INFO

Keywords:
Hydrogel
Organ-on-a-Chip
In silico modeling
3D tumor microenvironment
Glioblastoma
Hypoxia

ABSTRACT

Glioblastoma (GBM) is one of the most aggressive and lethal brain tumors, characterized by limited therapeutic options and poor prognosis. This condition is strongly linked to the limitations of current preclinical models: traditional two-dimensional cell cultures and animal models often fail to recapitulate the complexity of the tumor microenvironment (TME), resulting in limited predictive value for clinical outcomes. Here, a biomimetic three-dimensional (3D) *in vitro* culture system is presented, designed to incorporate key components of the TME and to mimic human GBM biology by: (i) employing ad hoc–designed hydrogels as extracellular matrix (ECM) equivalents; (ii) integrating multiple cell types, namely GBM cells and astrocytes; and (iii) implementing dynamic cell culture conditions through a custom-designed microfluidic platform that closely resembles the hypoxic conditions typically found in this tumor. In parallel, an *in silico* model is developed to evaluate key microfluidic parameters, including flow velocity, diffusive and convective transport within the system, and spatiotemporal oxygen distributions. Experimental validation combined with computational modeling enables optimization of device design and conditions to better replicate hypoxic GBM microenvironments. The GBM-on-Chip platform highlights the potential of advanced 3D systems to improve physiologically relevant *in vitro* cancer models and support future drug testing and therapy development.

1. Introduction

Glioblastoma (GBM) is the deadliest form of adult primary brain cancer, accounting for approximately 15% of all central nervous system (CNS) malignancies [1]. Currently, the standard-of-care therapy consists of the combination of maximal safe surgery resection, radiotherapy and chemotherapy, with Temozolomide (TMZ) being the gold standard drug [2]. Unfortunately, patients' survival time does not exceed 15 months, and only 26% of patients are expected to survive 2 years after treatment [3–6]. Despite several efforts in drug development over the past decades, little advances in the outcome for patients afflicted with GBM have been achieved. Immunotherapy, including CAR-T cell-based strategies and vaccine approaches, could represent a new promising therapeutic treatment, although the lack of GBM-specific antigens remains a limitation for their development and efficacy [7]. Unlike other solid tumors, the high mortality of GBM is not due to metastatic spread of cancerous cells in the body, but rather to the presence of therapy-resistant tumor cells able to infiltrate into the surrounding brain tissue, making complete extirpation impossible. These residual cells, localized at the resection margin, are often not identified by standard MRI imaging and neither treated properly by radiotherapy and chemotherapy leading to GBM recurrences after tumor resection [7,8]. Such

* Corresponding author. Institute of Nanotechnology, National Research Council (CNR-NANOTEC), c/o Campus Ecotekne, via Monteroni, Lecce, 73100, Italy.
** Corresponding author.Institute of Nanotechnology, National Research Council (CNR-NANOTEC), c/o Campus Ecotekne, via Monteroni, Lecce, 73100, Italy.
E-mail addresses: alessandro.polini@cnr.it (A. Polini), francesca.gervaso@cnr.it (F. Gervaso).
[1] G. Corallo, L. Sercia and A. De Giorgi contributed equally to this work as first authors.
[2] A. Polini and F. Gervaso contributed equally to this work as senior authors.

https://doi.org/10.1016/j.mtbio.2026.103548
Received 28 April 2026; Received in revised form 24 July 2026; Accepted 9 August 2026
Available online 11 August 2026

cells, together with the surrounding extracellular matrix (ECM), blood vessels, and healthy cells (including astrocytes, glutaminergic neurons and macrophages), constitute the tumor microenvironment (TME) [9–11]. The TME is responsible for inducing heterogeneity, plasticity and evolution in the cancer cell population, which in turn modifies and manipulates adjacent tumor niches [12]. Indeed, the limited efficacy of current GBM therapies is largely attributed to the high degree of intra- and intertumoral heterogeneity, as well as the complex interactions between tumor cells, stromal cells, and the ECM within the TME [13–15]. Consequently, the development and evaluation of new therapeutic strategies must focus on experimental platforms that closely replicate the GBM microenvironment to better understand tumor biology and accelerate the drug discovery and testing [16,17].

An ideal *in vitro* GBM model should be highly biomimetic, thus incorporating all crucial components of the TME, both in terms of 3D ECM organization, mechanical properties and cell populations, while remaining sufficiently simple to ensure reproducibility [5,18]. Mono-layer culture models, though still widely used to understand peculiar biological features of GBM, do not account for the TME and therefore do not allow to investigate the role of the different players in the tumorigenesis and expansion [4,19]. Given the severe limitations of 2D culture systems, the development of more physiologically relevant 3D models is required to recapitulate *in vitro* GBM growth and get further insights into its biology [20,21]. In this context, 3D cancer models such as spheroids and organoids are widely used, since they can recapitulate several tumor characteristics, including growth kinetics, cellular heterogeneity, signaling pathway activity, and gene expression [22]. However, these scaffold-free cell culture methods lack the cell-matrix interactions present in the native tumor stroma. The combination of spheroids with 3D culture systems, such as hydrogels and scaffolds, fills this gap, providing a platform able to recreate both cell-cell and cell-matrix interactions, while dynamically controlling chemokines and growth factors gradient, which are essential features for mimicking *in vivo* conditions [23,24]. Among the currently available 3D cell culture platforms, hydrogels have gained growing interest in the last years. They are hydrophilic polymer networks, capable of retaining large amounts of water, broadly used for their strong similarity to the natural ECM and their tunable physicochemical properties [12,20,25]. Deriving from natural ECM extracts, commercially available hydrogels, *e.g.* Matrigel, Cultrex, HyStem and Geltrex [26,27], are commonly used for their biological properties. However, their undefined composition, limited reproducibility, and high cost remain major drawbacks [22]. In contrast, natural polymer-based biomaterials, such as fibrin, albumin, collagen, hyaluronic acid, chitosan and gelatin, have been proposed as brain-mimetic matrices for GBM studies because of their tunable chemical and physical properties and their greater experimental consistency [28]. However, some of these materials, such as hyaluronic acid, although notably overexpressed in GBM ECM [29–33], intrinsically exhibit low mechanical strength and therefore do not fall within the target brain stiffness range, which spans from the very soft mechanical properties of healthy brain tissue (0.1–1 kPa) to the higher stiffness reported for GBM (up to ~13.5 kPa) [23,34]. Thus, to recreate 3D structures capable of covering the full physio-pathological spectrum of GBM stiffness, commonly used approaches rely on either covalently crosslinked or non-covalent hydrogel systems [22,35]. In this context, methacrylate gelatin (GelMA) offers several advantages in terms of stiffness modulation [28,36–41], while simultaneously offering favorable biological properties. Thanks to its abundance in arginine-glycine-aspartic acid (RGD) sequences and matrix metalloproteinase-responsive peptide motifs, GelMA promotes both cell–matrix adhesion and cell-mediated matrix remodeling [42–44]. Though less explored than GelMA, chitosan presents interesting features as a 3D culture system [45–47]. Chitosan is composed of randomly distributed D-glucosamine and N-acetyl-glucosamine monomers, and is chemically similar to glycosaminoglycans (GAGs), which are the major components of brain tumor ECM. In presence of weak bases, such as β-glycerophosphate, chitosan becomes a thermosensitive hydrogel, remaining liquid at low temperatures (8–25°C) and undergoing gelation at physiological temperature (37°C). This temperature-mediated sol-gel transition makes chitosan highly attractive for 3D *in vitro* models [22,24,35,48,49]. Since both GelMA and chitosan physical properties can be easily tuned by varying process parameters (*e.g.*, polymer concentration, gelling agent composition, time of physical stimulus exposure) [50], these materials were both selected in this study as potential ECM analogues to implement the three-dimensionality of the *in vitro* GBM model.

Another essential factor for improving the fidelity of *in vitro* GBM models is the inclusion of healthy, non-cancerous cells that surround and influence tumor behavior and progression. Among these, astrocytes are the most abundant parenchymal brain cells interacting with GBM cells, influencing tumor growth and invasion through both the secretion of soluble factors and direct physical contact. The latter is believed to be a major driving force behind astrocyte-mediated glioma cell migration and invasion [14,51,52]. Therefore, in the present study, malignant GBM cells and non-tumoral human astrocytes were both included in the model to assess their mutual interactions.

Finally, to more closely mimic *in vivo* cancer dynamics, a highly biomimetic GBM *in vitro* model should include proper cell and tissue perfusion through the implementation of a dynamic cell culture system. Such feature can be readily achieved using the Organ-on-Chip (OoC) technology, which, in addition to enabling fluidic control, offers several advantages over traditional *in vitro* models – such as miniaturization, reduced reagent consumption, and precise regulation of the cellular microenvironment – thus representing a powerful tool to investigate GBM progression, invasion, and therapy resistance [53,54]. Notably, GBM exhibits a highly heterogeneous and metabolically stressed microenvironment, marked by local regions of low oxygen tension [55–57]. Oxygenation within GBM is highly heterogeneous and exists along a continuum rather than as a single threshold. Physiological oxygen levels in the healthy brain are already considerably lower than atmospheric oxygen, typically ranging from approximately 4–6% O_2, depending on the brain region and local metabolic activity [56]. Within GBM, oxygen tension progressively decreases from relatively well-perfused peripheral regions toward poorly vascularized and peri-necrotic areas, generating spatial oxygen gradients that regulate tumor cell behavior. Accordingly, different oxygen thresholds have been proposed to define the severity of hypoxia. For example, mild hypoxia has been classified as 0.5–2.5% pO_2, moderate hypoxia as 0.1–0.5% pO_2, and severe hypoxia (or anoxia) as $\leq$0.1% pO_2, although these classifications may vary depending on the experimental methodology and biological endpoint evaluated [56]. More generally, oxygen concentrations between approximately 1 and 3% pO_2 are sufficient to activate hypoxia-responsive signaling pathways in many cell types [58], whereas the lowest oxygen levels are typically found in diffusion-limited, peri-necrotic niches characterized by metabolic adaptation, maintenance of glioma stem-like cells, and increased therapeutic resistance [59–61]. Therefore, oxygen concentrations below 1% pO_2 could be regarded as representative of the most severely hypoxic regions of GBM.

Several factors contribute to the development of hypoxia in GBM: (*i*) uncontrolled tumor-cell proliferation, which increases oxygen consumption, (*ii*) abnormal vascular endothelial growth factor (VEGF)-mediated neovascularization, which produces small, tortuous and frequently occluded vessels incapable of supplying adequate oxygen to the expanding tumor mass [62]. This chronic oxygen deprivation promotes genetic and phenotypic changes, favoring the rise of highly aggressive tumor cells able to infiltrate the surrounding healthy brain tissue [63]. Such genetic changes are due to the expression of a specific transcription factor, the hypoxia-inducible factor 1 alpha (HIF1α) [62,64], activated by a low partial pressure of O_2. Particularly, in hypoxia, HIF1α accumulates in the nucleus [65], where it becomes an active transcription factor that drives the expression of genes involved in angiogenesis, metabolic reprogramming, immunosuppression, and invasion [66,67].

Adopting an OoC approach facilitates the integration of all the aforementioned features into a single, highly biomimetic GBM model, potentially overcoming the limitations of conventional cell culture methods and animal models, which fail to reproduce TME complexity, raise ethical concerns, and exhibit interspecies variations—all factors that limit the model predictive value. Indeed, OoC platforms are already used for photodynamic therapy and magnetic hyperthermia testing [68, 69], as well as for multi-organ platforms designed to study inter-tissue interactions [70]. Although recent literature reports a rapid increase in GBM-on-Chip models that can significantly advance the knowledge of GBM etiology and revolutionize drug development, most of them focus on GBM interaction with the blood-brain barrier (BBB) and tumor vascularization, focusing on intravasation/extravasation processes, or cell invasion and metastasis [53,54,71–73]. In the present study, we aimed to improve the fidelity of GBM *in vitro* models by: *(i)* employing *ad hoc*–designed hydrogels with tunable physicochemical properties to recapitulate the GBM ECM organization and to investigate cell–ECM interactions; *(ii)* incorporating multiple cell types, namely GBM and astrocyte cells, to explore their reciprocal interactions; *(iii)* implementing dynamic cell culture settings through the design and microfabrication of a microfluidic platform that mimics *in vivo* hypoxic conditions of GBM tumor; and *(iv)* developing an *in silico* model of the microfluidic platform to reproduce and predict the physicochemical microenvironment under both static and dynamic perfusion conditions.

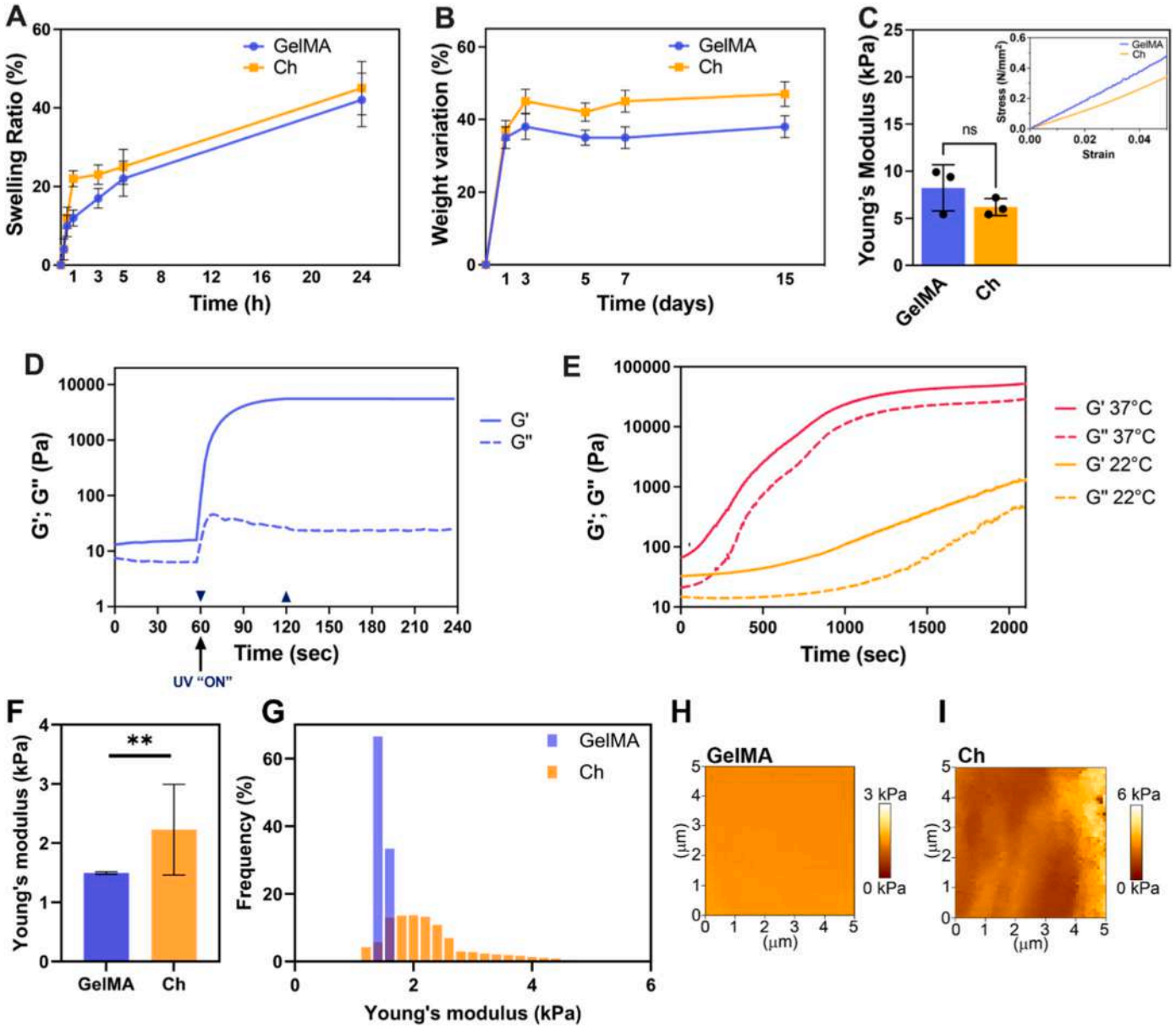

Fig. 1. Physicochemical characterization of GelMA and Ch hydrogels. A) Swelling ratio percentage of GelMA and Ch in PBS (n = 10). B) Stability test: weight variation over time of GelMA and Ch hydrogels immersed in PBS at 37°C (n = 10). C) Young's modulus calculated as the slope of the compressive stress-strain curve at low strain values performed on GelMA and Ch hydrogels (n = 3; ns: not significant). Inset: stress–strain compression curves. D) *In situ* gelation kinetics of 10% GelMA (logarithmic scale). Storage modulus: G′, solid line; loss modulus: G″, dotted line. UV light exposure was applied at t = 60 s and interrupted at t = 120 s (indicated by blue inverted triangles in the graph). E) Time sweep rheological analysis of the Ch hydrogel (logarithmic scale). G′ and G″ were measured as a function of time at 37°C (red lines) or 22°C (yellow lines). F) Young's modulus of GelMA and Ch and their frequency distribution (G) calculated from more than 15,000 data points, collected through force-distance measurements in QI mode AFM. H,I) Stiffness maps of GelMA (H) and Ch (I) acquired by QI mode AFM (5 × 5 μm^2, 112×112 pixels), with every pixel corresponding to a force/distance measurement. n = 3, images are representative of at least three independent samples. Data are presented as the mean ± SD. (For interpretation of the references to color in this figure legend, the reader is referred to the Web version of this article.)

In this study, hypoxia was reproduced through the chip's geometry and perfusion configuration, and validated both quantitatively, using an oxygen-sensitive fluorescent probe, and biologically, through the assessment of HIF1α accumulation. Together, these complementary approaches confirmed the *in silico* predictions of oxygen partial pressure within the microfluidic platform. Together, these complementary and integrated approaches enabled us to better understand how matrix composition and mechanical stimuli influence GBM cell growth and organization, providing insights into how more physiologically relevant *in vitro* platforms could enhance translational cancer research.

2. Results

2.1. Hydrogels characterization

With the aim of reconstructing the 3D spatial organization of GBM and developing biomimetic extracellular matrices that replicate the native mechanical and structural features of GBM, two hydrogel formulations, capable of encapsulating both GBM cells and astrocytes, were selected based on their physicochemical properties. The first hydrogel, GelMA 10% w/V, (hereafter abbreviated as GelMA) was prepared by mixing a gelatin methacrylate solution with a photoinitiator (lithium phenyl-2,4,6-trimethylbenzoylphosphinate, LAP) and exposing it to UV irradiation to induce crosslinking. The second hydrogel (hereafter referred to as Ch) consisted of a chitosan solution 3.33% w/V, which, when mixed with a gelling agent (β-glycerophosphate, BGP) and heated to 37°C, undergoes a sol–gel transition. Both hydrogels were subjected to comprehensive physicochemical characterization, including evaluation of swelling capacity, stability, and mechanical properties.

The capability of GelMA and Ch hydrogel to retain water was evaluated by a swelling test (Fig. 1A). Both formulations exhibited a similar swelling profile, showing an approximate 50% swelling ratio after 24 h. Moreover, the degradation profile of the hydrogels after immersion in phosphate-buffered saline (PBS) at 37°C demonstrates great long-term stability up to 15 days for both hydrogels (Fig. 1B). The mechanical characterization, evaluated by an unconfined compression test, is displayed in Fig. 1C. The stress-strain curve shows a linear elastic behavior in the range of interest namely from 1% to 5% of strain; indeed, the stiffness increases as the strain increases, showing the typical response of hydrogel materials (inset in Fig. 1C). Young's modulus, calculated as the slope of the compressive stress-strain curve at low strain values (in the range 1 – 5% of strain), was 8.2 ± 1.9 kPa and 6.2 ± 0.7 kPa for GelMA and Ch, respectively. No statistically significant difference was observed between the two materials, with both values falling within the reported range of human GBM tissue stiffness [34]. Dynamic rheological measures were performed to assess the viscoelastic behavior of the materials. A time sweep rheology test at a constant frequency of 1 Hz and 3% strain was conducted to demonstrate the UV-responsive behavior of GelMA (Fig. 1D). Prior to UV exposure, GelMA exhibited weak solid-like behavior ($G' > G''$), likely due to gelatin chain entanglements and partial gelation. Upon UV irradiation (60 s), a rapid increase in both moduli was observed, with G' remaining dominant and a G'/G'' ratio of approximately 100, indicating the formation of a chemically crosslinked elastic network. Besides, a time sweep test was conducted on Ch at a constant frequency of 1 Hz and 10% strain at 22°C (room temperature) or 37°C (gelation temperature) to investigate the thermoresponsive behavior of the material (Fig. 1E). Under both temperature conditions, the storage modulus (G') remained consistently higher than the loss modulus (G''), indicating a predominantly solid-like response. Notably, the test conducted at 37°C exhibited a markedly higher increase in G' compared to that at 22°C, suggesting enhanced network formation at physiological temperature.

Mechanical properties of the two hydrogels were further evaluated by high-resolution force–distance measurements using atomic force microscopy (AFM) in Quantitative Imaging (QI) mode (Fig. 1F–I). These measurements revealed lower Young's modulus values for both hydrogels (1.49 ± 0.02 and 2.23 ± 0.77 kPa for GelMA and Ch, respectively) than those obtained from bulk compression tests. Interestingly, the analysis of the Young's modulus distribution, expressed as frequency (%) (Fig. 1G), revealed a remarkably homogeneous stiffness distribution in the GelMA substrates, as further confirmed by the uniform color pattern in the corresponding stiffness map (Fig. 1H). In contrast, the Ch samples exhibited a broader Young's modulus distribution and a more heterogeneous stiffness map (Fig. 1I), indicating spatial variability in their surface mechanical properties. The same analysis was performed on hydrogel cross-sectional slices obtained by sectioning the bulk hydrogel cylinder (Fig. S1A), enabling AFM indentation of the hydrogel interior and, consequently, the assessment of its internal mechanical properties. The measurements revealed slightly higher Young's modulus values than those measured at the surface (3.33 ± 0.39 kPa and 2.38 ± 1.52 kPa for GelMA and Ch, respectively; Fig. S1B and C). Consistent with the surface analysis, Young's modulus distribution of Ch was broader than that of GelMA (Fig. S1D), indicating less homogeneous mechanical properties. Although a significant difference in surface stiffness was measured between the two hydrogel formulations, cross-sectional analysis revealed no significant differences in their Young's modulus. Because the cells are embedded within the hydrogels, the cross-sectional measurements more accurately reflect the mechanical environment experienced by the cells, indicating that both hydrogel formulations provide comparable mechanical conditions.

2.2. GelMA and Ch hydrogels allow for high cell viability and proliferation

The biocompatibility of the two hydrogel formulations toward both U87-MG human glioblastoma and SVG-A human astrocyte cell lines was assessed by means of a live and dead assay (Fig. 2A and B). Only a few red nuclei, indicative of dead cells, were detected in both matrices, confirming high cell viability over seven days of culture. Nevertheless, an increase in cell death was observed after seven days of culture for SVG-A cells, likely due to the spheroid size limiting oxygen and nutrient diffusion to the core, leading to the formation of inner necrotic regions. Interestingly, when SVG-A cells were co-encapsulated with U87-MG glioblastoma cells, overall cell viability increased, despite spheroid formation.

The U87-MG and SVG-A cell proliferation within both hydrogels was also evaluated, to assess cell metabolic activity and obtain quantitative information on cell viability (Fig. 2C). On day 1, U87-MG cells encapsulated within the GelMA hydrogel exhibited higher metabolic activity with respect to SVG-A cells. This trend was reversed on day 3, when U87-MG cells proliferation slightly decreased, while SVG-A metabolism increased up to day 7. The co-culture condition displayed an intermediate metabolic profile, consistent with the combined contribution of both cell lines. Notably, both U87-MG and SVG-A cells showed a higher metabolic activity when encapsulated within the Ch hydrogel from day 1 onward, compared to GelMA. In Ch, U87-MG cells' metabolism remained stable over the entire 7-day culture period, while SVG-A cells showed a considerable increment in their metabolism at day 3, followed by a decrease, likely connected to cell death increasing due to the necrotic core formation within the spheroids. Similarly, in co-culture conditions, cells encapsulated within the Ch hydrogel showed comparable metabolic activity at days 1 and 7, with a peak at day 3, suggesting enhanced interaction between the two different cell lines promoted by the Ch matrix.

2.3. Hydrogel formulation strongly influences cell morphology

Hydrogel-embedded U87-MG and SVG-A cells were subjected to DAPI/phalloidin staining to evaluate and compare their morphology and distribution inside the two matrices (Fig. 3A). Following 8 days of culture, U87-MG cells encapsulated in GelMA displayed an elongated morphology, closely resembling the phenotype typically observed when

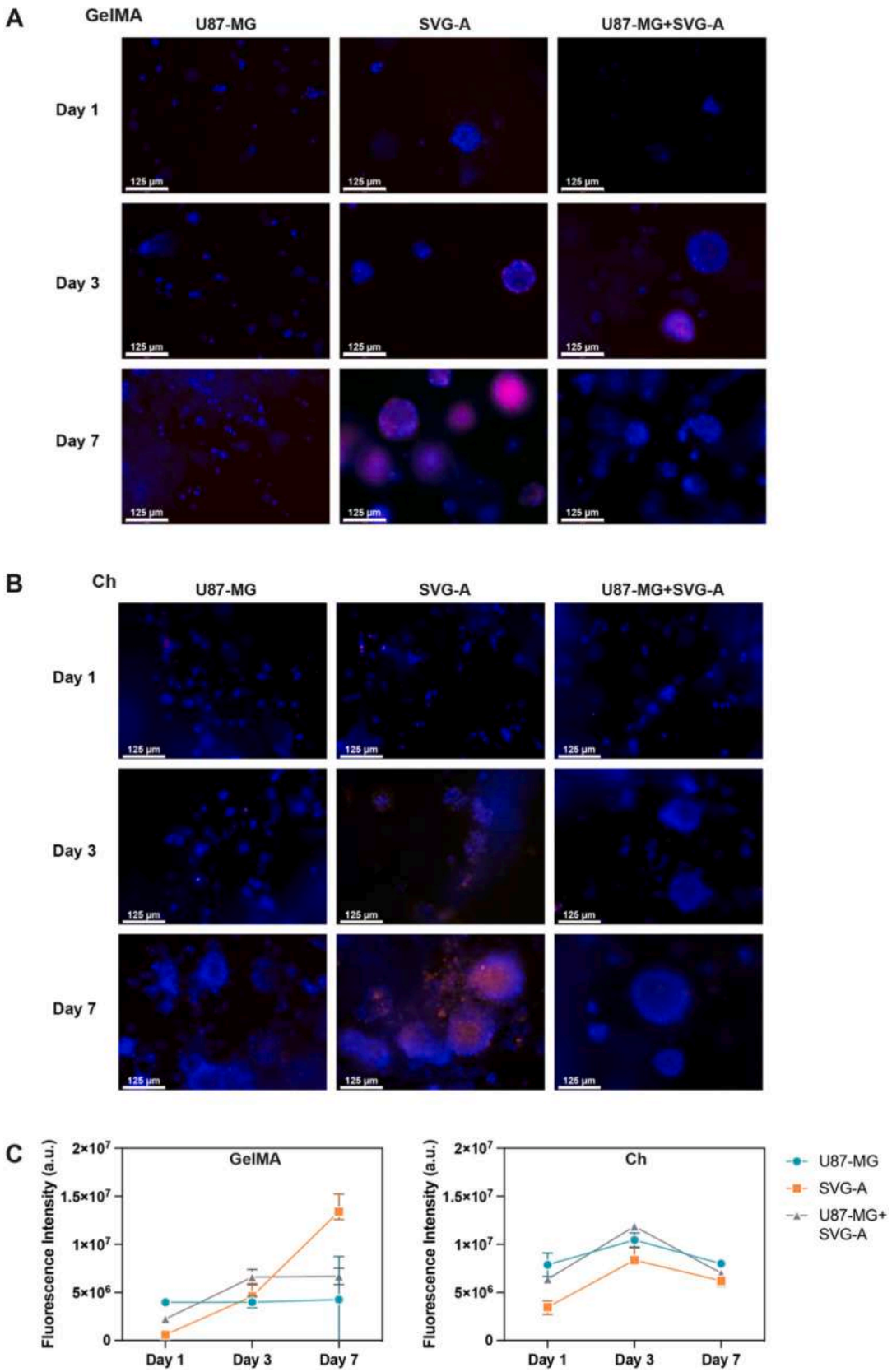

Fig. 2. Live and dead analysis and Presto Blue assay of cells embedded in hydrogel drops. A, B) Live and dead analysis of mono-culture (U87-MG or SVG-A) and co-culture (U87-MG + SVG-A) models obtained with cells embedded in GelMA (A) and in Ch (B) hydrogel drops. NucBlue reagent (blue) stains cell nuclei, propidium iodide (red) stains dead cells. Scale bars: 125 µm. (n = 3, images are representative of at least three independent samples). C) Presto Blue assay of mono-culture (U87-MG or SVG-A) and co-culture (U87-MG + SVG-A) models obtained with cells embedded in GelMA (left) or Ch (right) hydrogel drops analyzed at days 1, 3 and 7 of culture. Data are presented as the mean ± SD. (For interpretation of the references to color in this figure legend, the reader is referred to the Web version of this article.)

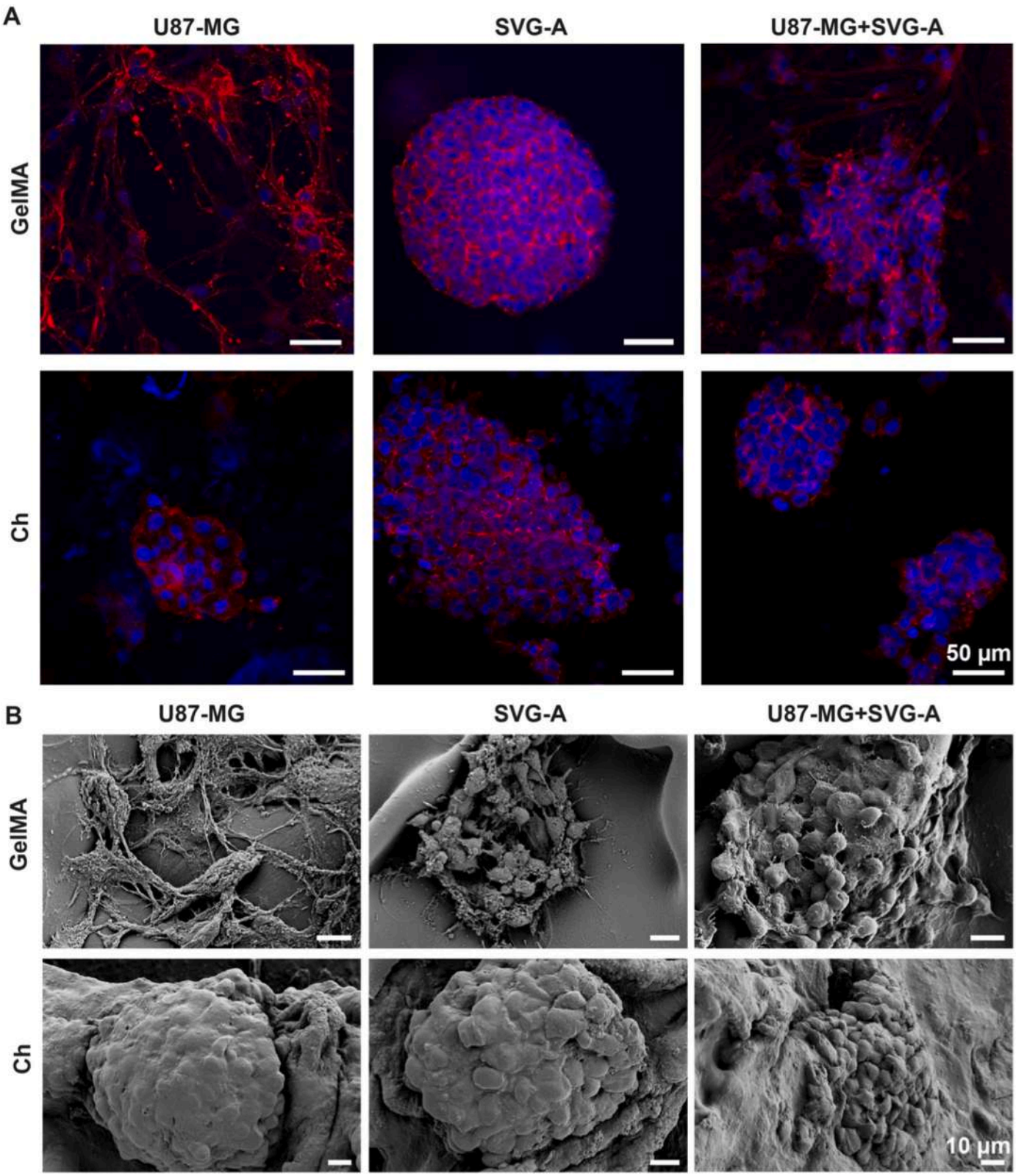

Fig. 3. Morphological analysis of U87-MG and SVG-A cells embedded in hydrogel drops after 8 days of culture. A) DAPI/Phalloidin-TRITC staining of U87-MG and SVG-A cells embedded in GelMA hydrogel (top) and Ch hydrogel (down) drops in mono-culture and in co-culture models. Phalloidin labels F-actin (red), while DAPI stains cell nuclei (blue). Scale bar: 50 μm. B) SEM micrographs of U87-MG and SVG-A cells embedded in GelMA hydrogel (top) and Ch hydrogel (down) drops in mono-culture and in co-culture models. Scale bar: 10 μm. (n = 3, images are representative of at least three independent samples). (For interpretation of the references to color in this figure legend, the reader is referred to the Web version of this article.)

cultured on plastic substrates. On the other hand, SVG-A cells aggregated inside the hydrogel, forming large spheroids, reaching a diameter up to 300 μm at day 8 of culture. Under co-culture conditions, in the GelMA hydrogel, a hybrid behavior was observed, characterized by the presence of both elongated cells and spheroids with irregular morphology, compared to those observed in monocultures. In contrast, when cultured in Ch hydrogels, both U87-MG and SVG-A cells predominantly formed spheroids in both mono- and co-culture models.

To gain further insight into cells distribution within the GelMA and Ch hydrogels, samples of cell-laden hydrogels were analyzed by scanning electron microscopy (SEM) after 8 days of culture (Fig. 3B). U87-MG cells clearly exhibited distinct behaviors within the two matrices, displaying an elongated morphology within the GelMA hydrogel and forming spheroid-like aggregates within the Ch hydrogel. SVG-A cells, although forming spheroids in both matrices, showed slightly different characteristics. Specifically, spheroids formed within GelMA appeared less compact, suggesting that the cells might interact more extensively with the biomaterial, compared to those in the Ch hydrogel. In co-culture conditions, a similar trend to mono-culture is observed, with GelMA-embedded cells showing enhanced matrix adhesion and decreased cell aggregation. These findings led us to hypothesize that U87-MG cells retain their behavior in the GelMA hydrogel even in the co-culture model, remaining as single cells and interacting more with the matrix compared to the SVG-A cell population. To further test this hypothesis, we performed immunofluorescence staining using cell-specific markers to better distinguish the two cell populations within the hydrogel matrix.

2.4. Ch hydrogel induces the formation of heterotypic spheroids

Cell-specific markers were used to further investigate spheroids composition. To this end, an immunofluorescence staining was performed using CD44, a type I single-pass transmembrane glycoprotein with a pro-tumorigenic effect [74,75] as U87-MG cell marker, and GFAP, an astrocyte-specific intermediate filament protein as astrocytic cell marker. Marker specificity was validated by immunofluorescence staining of 2D cultures of U87-MG and SVG-A cells, respectively, confirming the absence of cross-reactivity (Fig. S2). Both markers were applied in mono- and in co-culture hydrogel models. As shown in Fig. 4, in the GelMA co-culture model, U87-MG cells arrange themselves to form a network surrounding SVG-A spheroids. In contrast, in the Ch co-culture model, both U87-MG and SVG-A cells interact with each other to form spheroids consisting of a mixed population of the two cell types.

2.5. Ch hydrogel stimulates spheroid growth more effectively than GelMA hydrogel

Brightfield images of U87-MG and SVG-A cells embedded in hydrogel drops were acquired and further analyzed to evaluate spheroid growth under static 3D culture conditions. As shown in Fig. 5, although both hydrogel formulations contained a similar number of cell aggregates (approximately 100 spheroids per 40 μL drop), a marked difference in their sizes was observed. In particular, the total area of cell aggregates in the Ch hydrogel is 4.5 times greater than in the GelMA hydrogel (Fig. 5B). Quantitative analyses were performed on three

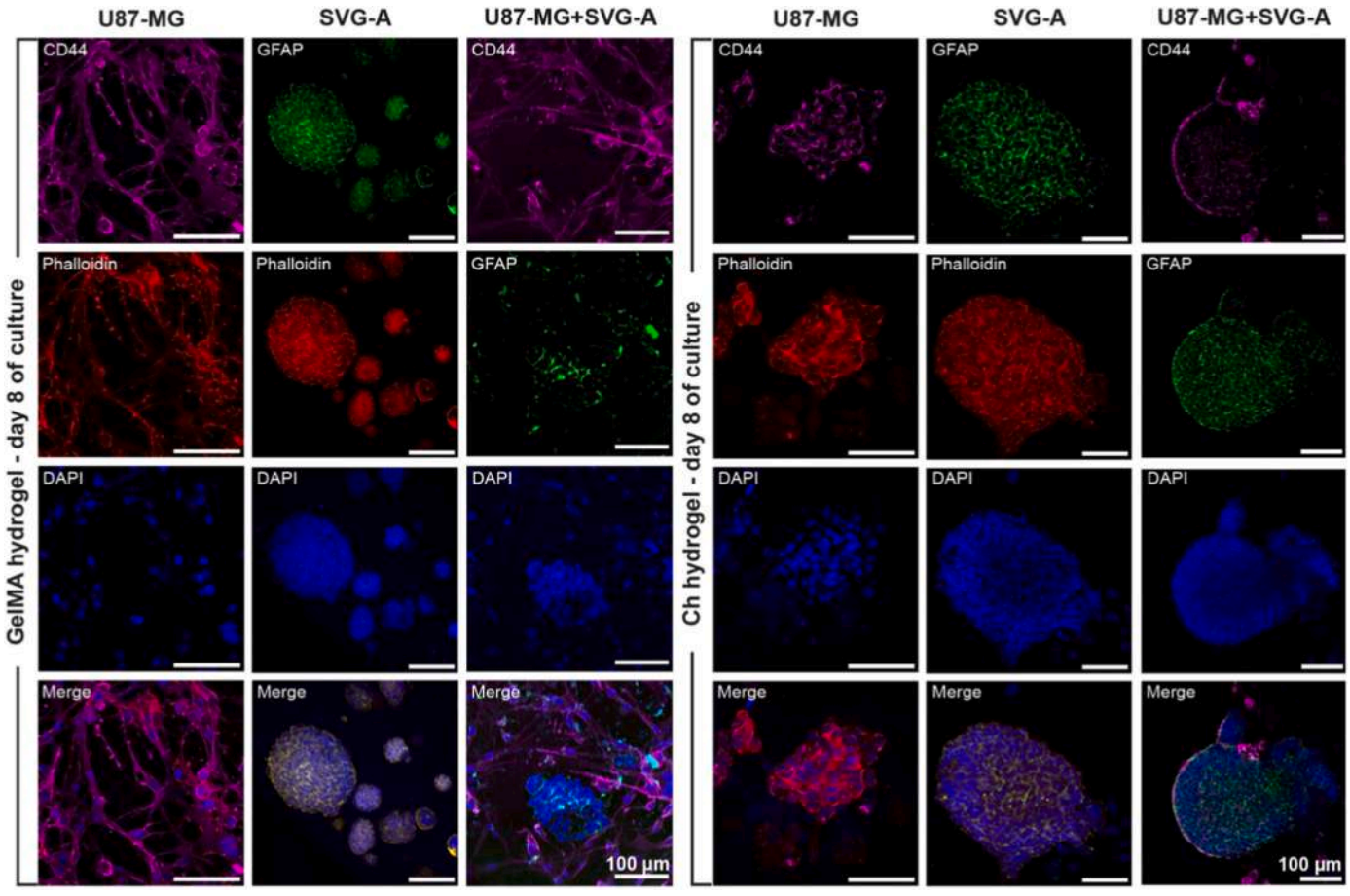

Fig. 4. Immunofluorescence staining U87-MG and SVG-A cells embedded in hydrogel drops after 8 days of culture. Representative images of immunofluorescence analysis of U87-MG and SVG-A cells embedded in GelMA hydrogel (left) and Ch hydrogel (right) drops in mono-culture and in co-culture models after 8 days of culture. DAPI (blue) stains nuclei. Scale bars: 100 μm (n = 3, pictures are representative of what was observed in at least three independent samples or replicates). (For interpretation of the references to color in this figure legend, the reader is referred to the Web version of this article.)

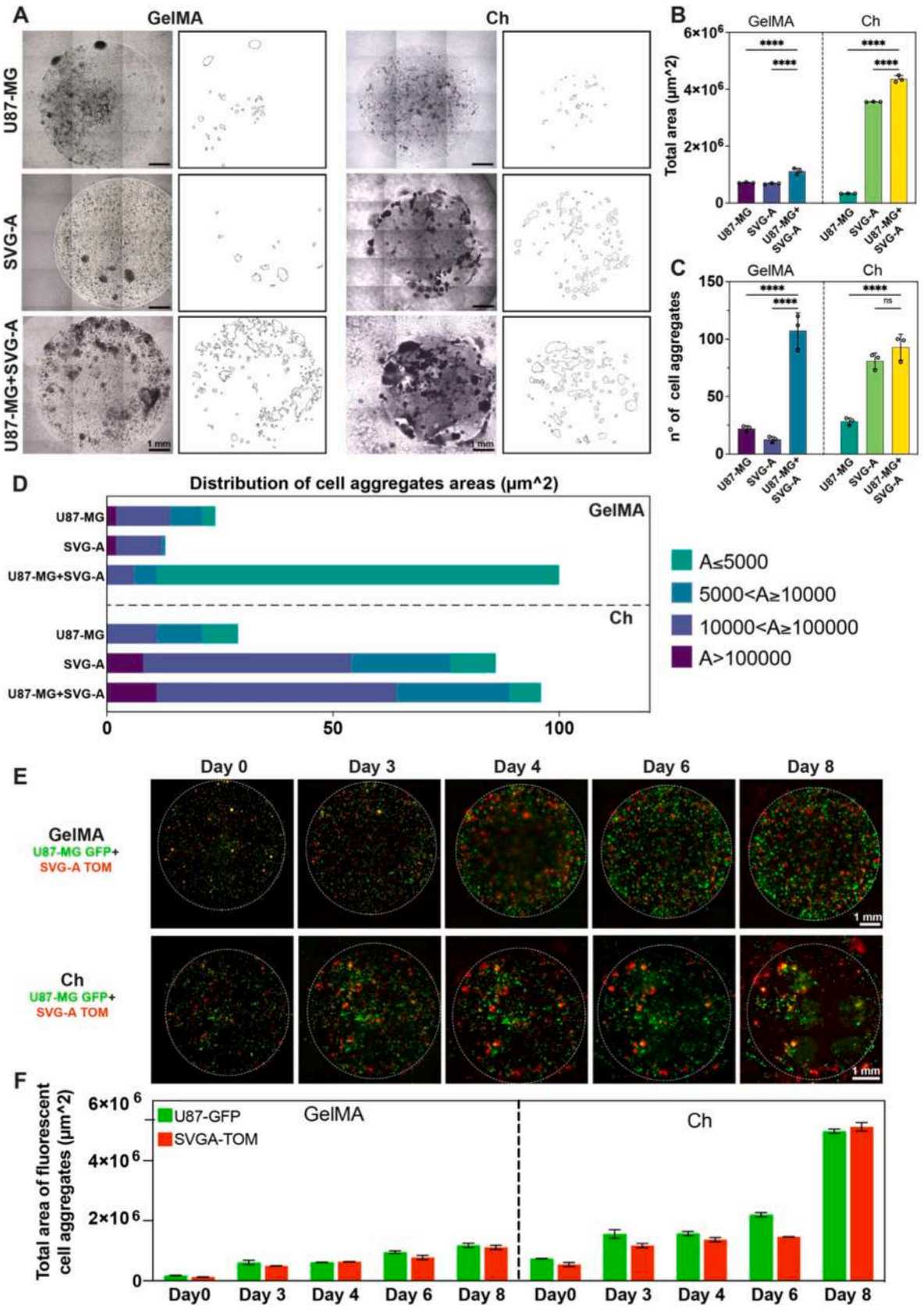

(caption on next page)

Fig. 5. Live-cell imaging of U87-MG and SVG-A cells embedded in hydrogel drops at day 8 of culture. A) Representative brightfield images of U87-MG and SVG-A cells embedded in GelMA (left) and Ch hydrogel (right) drops in mono- and co-culture models after 8 days. Scale bars: 1 mm. To the right of each micrograph, a black and white image that evidences the spheroids borders is reported, obtained using imageJ software. Image analysis of the total area (B), numbers (C), and areas distribution (D) of cell aggregates, performed on brightfield micrographs (n = 3, images are representative of three independent experiments). Data are presented as the mean ± SD from three independent experiments (n = 3). Each dot represents one replicate. E) Representative fluorescent micrographs of transfected GFP-U87-MG and TOMATO-SVG-A cells (co-culture) embedded in GelMA (top) and Ch (down) hydrogel drops automatically acquired at days 0, 3, 4, 6 and 8 of culture. Scale bars: 1 mm. The entire drop is outlined by a white dashed circle. F) Image analysis of the cell aggregates area performed on fluorescent micrographs at day 0, 3, 4, 6 and 8 (n = 3, images are representative of three independent experiments). Green bars indicate U87-MG GFP cells, while red bars indicate SVG-A TOMATO cells. Data are presented as the mean ± SD from three independent experiments (n = 3). (For interpretation of the references to color in this figure legend, the reader is referred to the Web version of this article.)

independent experiments (n = 3), demonstrating the reproducibility of spheroid formation. Consistently, the coefficient of variation (CV) of the mean spheroid area across experimental replicates was low, ranging from 2.7%, 3.2%, and 9.3% for U87-MG, SVG-A, and U87-MG + SVG-A co-cultures in GelMA, respectively, and from 1.9%, 0.2%, and 2.8% for the corresponding cultures in the Ch hydrogel, indicating good experimental reproducibility despite the intrinsic heterogeneity in spheroid size. Notably, measuring the size distribution of cell aggregates, most of them in the GelMA hydrogel are smaller or equal to 5000 μm^2, whereas in the Ch hydrogel, aggregate sizes can be up to 20 times larger (Fig. 5D). These findings clearly indicate that only the Ch hydrogel promotes enhanced interactions between U87-MG and SVG-A cells, leading to increased spheroids growth (Fig. S3).

To further validate this hypothesis and quantify the ratio between the two cell populations during spheroid formation in the static culture condition, we analyzed spheroid growth in both hydrogel formulations using live fluorescently labeled cells (Fig. 5E). Specifically, U87-MG and SVG-A cells were transfected with plasmids encoding GFP and TOMATO, respectively, enabling selective visualization and live tracking. Live cell imaging of these fluorescent cells embedded in hydrogel drops revealed that both cell types exhibited similar growth dynamics over the 8-day culture period (Fig. 5E and F). Notably, analysis of the fluorescent signal areas showed that cell aggregates consistently occupied a larger area in the Ch hydrogel compared to GelMA, corroborating our previous observations.

2.6. The in silico model predicts optimal conditions for dynamic culture in ad-hoc designed microfluidic device

Once ECM-equivalent hydrogels capable of supporting the static co-culture of GBM and astrocyte cells were assessed, an *ad hoc* chip was designed to implement a dynamic culture of the 3D GBM model. A circular-shape microfluidic platform was designed presenting a central channel crossing a circular well capable of hosting the cell-laden hydrogel in its inner part (Fig. 6A). The circular well is surrounded and delimited by a pillar-based crown, that simultaneously provides the surface tension required to keep the hydrogel confined within its region and allows the media flow to perfuse the hydrogel matrix, supplying the cells with essential nutrients (Fig. S4, Fig. S5). By sealing the chip with a polydimethylsiloxane (PDMS)/polystyrene (PS) cover secured by six screws, media leakage was prevented during the dynamic culture.

With the aim of predicting the optimal conditions for cell culture in the *ad hoc* designed microfluidic device, an *in silico* model of the chip was developed by importing the CAD geometry into COMSOL Multiphysics (Fig. 6B, top). A preliminary analysis on Reynolds number confirmed laminar flow conditions within the chip, consistent with microfluidic systems [76]. The geometry was discretized using the COMSOL built-in mesh generator, which provided a high-quality mesh (Fig. 6B, bottom) suitable for the simulations. First, the results regarding the laminar flow were analyzed, imposing a flow rate of 100 μL/h at the inlet. Specifically, the fluid velocity streamline was plotted within the chip (Fig. 6C), showing a symmetric flow behavior in both the microchannels and a high velocity reduction within the central well due to the presence of the hydrogel which hinders the flow. To quantify these considerations, a one-dimensional (1D) cut line was taken at the middle of the device, and the total velocity magnitude was plotted for both the GelMA and Ch setups (Fig. 6D). It is possible to appreciate the parabolic profile at the edges, which corresponds to the crown surrounding the well. This profile was expected since it is typical of the laminar regime, in which the flow is higher at the center and the lowest at the walls. On the other hand, the velocity inside the well is effectively negligible due to the hydrogel presence, demonstrating that in this region oxygen and nutrients will move *via* diffusion rather than convective flux. Only minor discrepancies were observed between the GelMA and Ch modelling setups. The slightly higher peaks when considering GelMA hydrogel are likely due to its lower porosity (0.80 ± 0.03 for GelMA and 0.95 ± 0.02 for Ch) and permeability ($4.1 \pm 0.6 \times 10^{-16}$ m^2 for GelMA and $1.2 \pm 0.4 \times 10^{-14}$ m^2 for Ch, Fig. S6), which further restrict fluid flow within the well and, in turn, enhance the flow in the surrounding crown. These data were corroborated by the experimental set-up, showing a high viability of U87-MG cells within the entire microwell of the chip when perfused with a 100 μL/h flow rate (Fig. S7).

To validate the mass-transport model, an acellular diffusion experiment was performed for both matrices. A rhodamine 6G solution was perfused through the device and its penetration into the hydrogel well was monitored over time by fluorescence microscopy, then compared with the concentration field predicted by the model using the corresponding diffusion coefficients (Fig. 6E–H). For both hydrogels the computed normalized-concentration maps and the temporal concentration profiles closely reproduced the experimental data, with $R^2 = 0.99$ for GelMA (Fig. 6E,F) and $R^2 = 0.94$ for Ch (Fig. 6G and H). Consistent with the higher porosity and permeability measured for Ch, the dye front advanced faster in the Ch than in GelMA, and this difference was correctly captured by the model. The slightly lower agreement obtained for Ch is attributable to the diffusion coefficient adopted for this matrix: whereas a rhodamine-specific value was available for a gelatin-based hydrogel [77], no direct measurement exists for rhodamine in Ch, and the coefficient was therefore estimated by scaling the free-water value through an obstruction factor derived from small-molecule diffusion data in Ch gels [78] (see **Methods** section). Overall, the good agreement between computed and experimental transport confirms the reliability of the diffusion model underpinning the subsequent oxygen-consumption simulations.

2.7. In silico modelling of oxygen-consumption predicts hypoxia development in the GBM-on-chip system

Subsequently, laminar flow was coupled with mass transport to evaluate and predict oxygen consumption within the hydrogel domain. In this extended model, the PDMS membrane and the PS cover were also included in the computational domain to account for oxygen diffusion and permeation from the external atmosphere through these layers, in addition to convective supply from the perfused medium. Cellular oxygen consumption within the hydrogel was described by Michaelis–Menten kinetics along with a cellular growth law (see **Methods** section) and two experimental protocols were simulated: 4 days of static culture followed by 4 days of dynamic perfusion (4S+4D), and 8 days of continuous perfusion from seeding (8D), both at a flow rate of 100 μL/h. Simulation results showed distinct mean pO_2 time courses between the two protocols (Fig. 7A and B). In the 4S+4D condition, during the initial

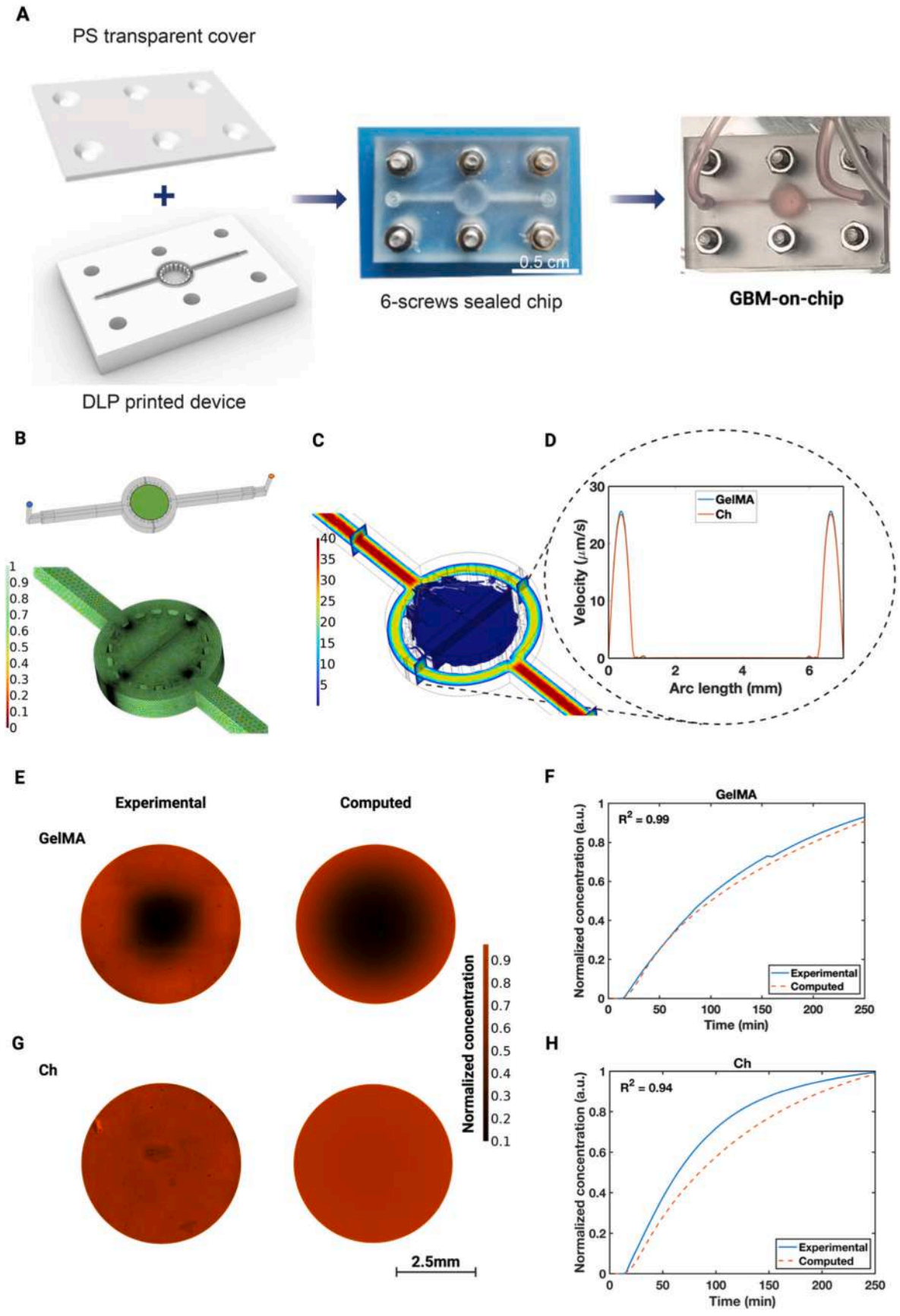

(caption on next page)

Fig. 6. GBM-on-Chip device development and computational setup. A) GBM-on-Chip fabrication and assembly. B) 3D chip geometry imported into COMSOL Multiphysics (blue: inlet, orange: outlet, green: hydrogel domain) and the corresponding mesh quality illustrated by mesh skewness distribution. C) Velocity streamlines (μm/s) with representative *yz* cross-sectional slices. D) 1D cut line of velocity profile along the mid-plane of the device. E–H) Validation of the diffusion model against experimental rhodamine transport. E) Experimental (left) and computed (right) normalized rhodamine 6G concentration maps in the GelMA-filled chamber; scale bar 2.5 mm. F) Corresponding experimental (solid) and computed (dashed) normalized concentration over time for GelMA ($R^2 = 0.99$). G) Experimental (left) and computed (right) normalized rhodamine 6G concentration maps in the Ch-filled chamber; scale bar 2.5 mm. H) Corresponding experimental (solid) and computed (dashed) normalized concentration over time for Ch ($R^2 = 0.94$). (For interpretation of the references to color in this figure legend, the reader is referred to the Web version of this article.)

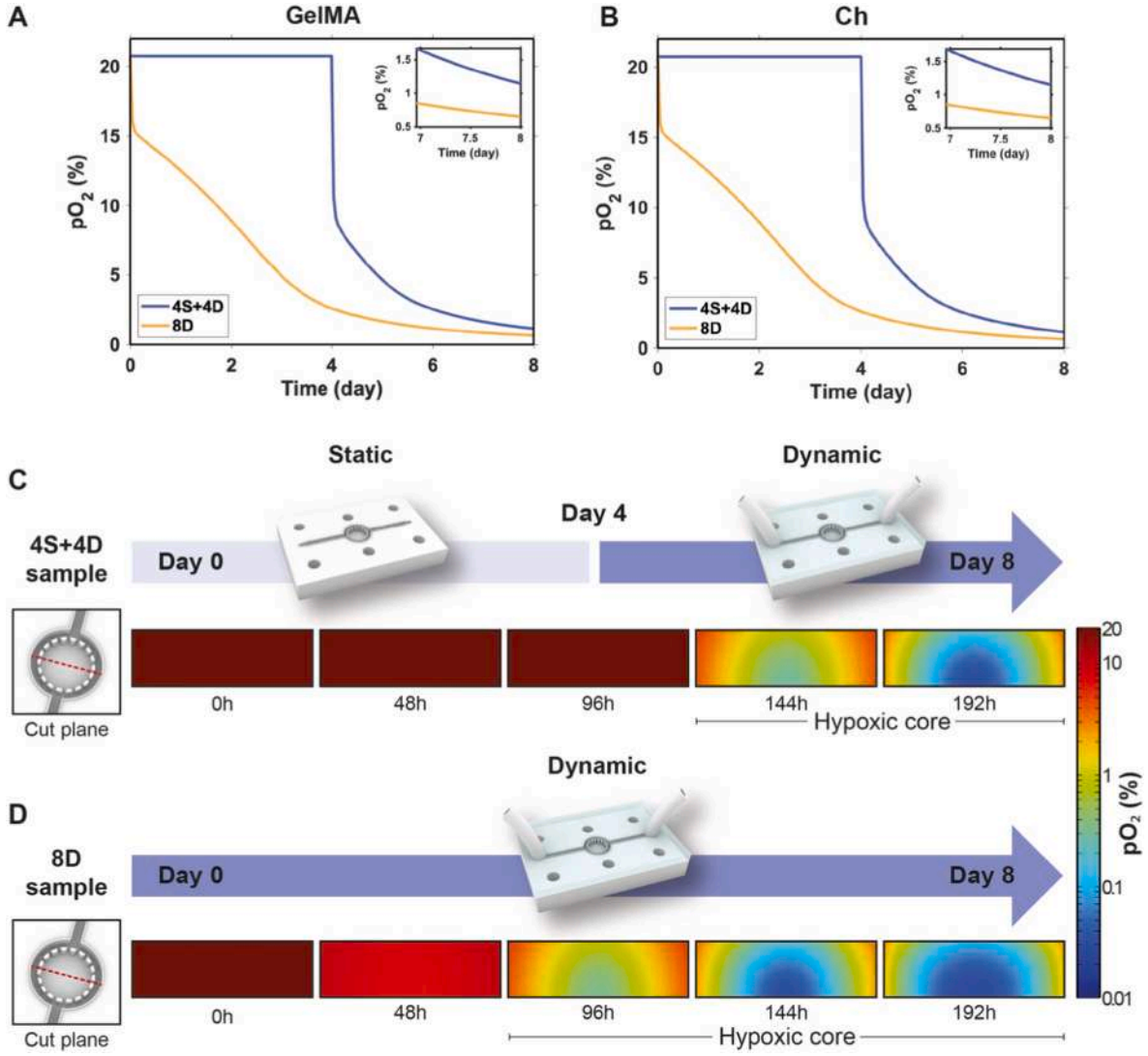

Fig. 7. *In silico* oxygen-consumption outcomes within the GBM-on-Chip platform. A-B) Time evolution of the mean oxygen partial pressure (pO_2) within the hydrogel phase for GelMA (A) and Ch (B) matrices, considering two culture protocols: 4 days of static conditions followed by 4 days of continuous perfusion (4S+4D) or 8 days of continuous perfusion (8D). Insets show a magnification of the final phase of the curves (days 7-8). C-D) Spatial distribution maps of pO_2 (logarithmic scale) within the chip (considering a specific cut plane indicated by the red dashed line) at selected time points for the 4S+4D condition (C) and the 8D condition (D). (For interpretation of the references to color in this figure legend, the reader is referred to the Web version of this article.)

static phase the chip remains open and equilibrated with atmospheric oxygen, maintaining pO_2 close to 21%. After day 4, once the device is closed with the PDMS/PS cover *via* 6 screws and connected to perfusion, the average pO_2 progressively decreases as cellular consumption overcomes oxygen replenishment, eventually reaching 1.09% at day 8. In contrast, in the 8D condition oxygen depletion begins immediately, as the chip is closed and perfused from the start; the system therefore spends a longer cumulative time at low oxygen levels and attains an even lower final pO_2 of 0.65%. Thus, while both protocols drive the construct into the hypoxic range [79], the 8D regime establishes a more pronounced and sustained hypoxic environment than 4S+4D condition (insets in Fig. 7A and B). Similar trends were obtained for both hydrogels (GelMA and Ch), consistent with preliminary fluid-dynamics simulations that predicted negligible differences in their respective velocity fields (Fig. 6D). To further examine oxygen heterogeneity, spatial maps of pO_2 were evaluated by drawing 2D cut planes within the hydrogel domain (Fig. 7C and D). In both protocols, a hypoxic core developed within the hydrogel, although its onset occurred earlier in the 8D condition than in 4S+4D, in agreement with the temporal evolution of mean oxygen levels. Notably, in both cases the minimum oxygen

concentration localized toward the central–bottom region of the construct. This pattern reflects the combined boundary conditions of the system: oxygen is supplied near the upper surface by diffusion through the PDMS/PS cover and along the periphery by the perfused medium in the surrounding crown, leaving the central–bottom region of the hydrogel as the most diffusion-limited. To quantify the contribution of the sealing configuration, we surface-integrated the net oxygen flux entering through the air-exposed PDMS/PS surfaces at day 8 and closed a global oxygen balance for the device (Fig. S8). Diffusion through the cover delivered approximately 9.9×10^{-13} mol/s, corresponding to approximately 19% of the integrated cellular oxygen demand (5.1×10^{-12} mol/s), a further 77% being provided by net perfusion, with the balance closing to within approximately 4% (transient oxygen depletion still ongoing at day 8). The oxygen distributions computed within the PDMS membrane and the PS cover are consistent with this result, showing near-atmospheric pO_2 across most of the two layers, a localized depletion mirroring the underlying cell chamber, and a gradient tracing the outlet channel, except for the air-exposed PS top surface which remains essentially uniform, consistent with its barrier-like low oxygen permeability. This modest but non-negligible atmospheric contribution, entering preferentially near the upper surface, accounts for the slight vertical oxygen asymmetry of the hypoxic core.

Overall, these *in silico* simulations quantitatively predict the formation of hypoxic cores in both culture protocols and indicate that the 8D condition yields a more severe and long-lasting hypoxic microenvironment for the chosen device geometry and perfusion parameters. These predictions guided the subsequent experimental studies aimed at validating hypoxia development within the GBM-on-Chip system.

2.8. Experimental oxygen mapping validates computational predictions of temporal and spatial hypoxia in the GBM-on-chip system

To experimentally validate the oxygen concentrations predicted by the computational model, the oxygen-sensitive fluorescent probe Image-iT™ Green Hypoxia Reagent was calibrated under controlled oxygen conditions using U87-MG/SVG-A co-cultures embedded in GelMA and Ch hydrogels (Fig. S9). The resulting hydrogel-specific calibration equations enabled conversion of fluorescence intensity into local oxygen partial pressure (pO_2) within the GBM-on-Chip, allowing direct comparison between experimental measurements and the simulated oxygen profiles. Temporal oxygen quantification revealed a progressive decrease in pO_2 throughout the culture period for both GelMA and Ch hydrogels under the two culture protocols (Fig. 8A–D). In both materials, experimental measurements closely followed the simulated oxygen depletion, accurately reproducing the distinct temporal profiles associated with the 4S+4D and 8D culture conditions. Oxygen levels progressively declined during culture, dropping below 5% after day 4 and reaching severe hypoxic conditions by day 8.

To further validate the model, spatial oxygen distribution was experimentally assessed by quantifying pO_2 in three predefined regions of the hydrogel compartment (outer left, Region 1; center, Region 2; and outer right, Region 3; Fig. 8E). Representative fluorescence images are shown in Fig. S10, while the corresponding quantitative analysis is presented in Fig. 8F and G. Experimental pO_2 measurements closely reproduced the spatial oxygen gradients predicted by the simulations, with the lowest oxygen concentrations consistently detected in the central region of the construct.

Overall, experimental oxygen concentrations showed excellent agreement with the computational predictions, with a maximum root mean square error (RMSE) of approximately 0.5% pO_2, confirming the ability of the computational model to accurately describe both the temporal evolution and spatial distribution of oxygen within the GBM-on-Chip system.

2.9. Dynamic culture conditions exert distinct effects on spheroid formation depending on the hydrogel formulation

U87-MG and SVG-A cells, embedded in both GelMA and Ch, were co-cultured for 8 days in the GBM-on-Chip device under dynamic culture conditions sustained for 4 or 8 days through continuous medium perfusion at 100 μL/h using a syringe pump. Cell morphology and distribution were analyzed through immunofluorescence (Fig. 9). Cell aggregation was mostly observed in the Ch hydrogel, particularly under dynamic culture conditions beginning on day 4 after seeding (Ch 4S+4D), similarly to what was noted under static conditions (Fig. 5 and Fig. S3). In contrast, cells cultured in the GelMA hydrogel within the GBM-on-Chip system largely remained as dispersed single cells. These observations are quantitatively supported by analysis of fluorescent micrographs (Fig. 9C–E). Indeed, both the mean aggregate area and the average number of cell aggregates at day 8 are significantly higher in Ch-Chip cultured under dynamic conditions after an initial 4-days static phase (Ch 4S+4D) compared with all other samples. Furthermore, the distribution of aggregate areas highlights a clear distinction between the matrices: in GelMA-Chips, most aggregates are smaller than 500 μm^2, which corresponds to the size of single cells or doublets, whereas in Ch-Chips, aggregates can reach areas nearly 10- to 100-fold larger, ranging from 5000 to 50,000 μm^2. This difference in spheroid formation may be attributed to the distinct ability of each hydrogel matrix to retain cell-secreted factors that promote cell aggregation in the presence of medium flow. Indeed, while GelMA supports spheroid formation under static conditions, the resulting spheroids are smaller than those formed in Ch, and this capability is further diminished under dynamic conditions.

Moreover, while the computational model was experimentally validated through quantitative oxygen mapping (Fig. 8), HIF1α immunostaining, a well-established marker of cellular hypoxic response, confirmed that the predicted hypoxic microenvironment elicited the expected biological response in cells cultured in the GBM-on-Chip system (Fig. 10). Quantitative analysis of fluorescence micrographs revealed significantly higher HIF1α expression at day 8 in cells cultured under continuous dynamic perfusion (8D) than in those exposed to dynamic flow only after an initial 4-day static phase (4S+4D), regardless of the hydrogel composition. In contrast, HIF1α expression was negligible under static culture conditions, consistent with the maintenance of oxygen partial pressures close to atmospheric levels (~21% pO_2).

3. Discussion

Development of innovative technologies in the field of precision medicine has improved the outlook for human tumor treatments, although, in the case of GBM, substantial challenges remain. GBM is among the most treatment-resistant tumors in adults. Surgical resection, radiation, and chemotherapy with temozolomide (TMZ) remain insufficient. As a result, the five-year survival rate of patients remains unacceptably low. Accurately recreating the GBM TME *in vitro* is essential for understanding its aggressive behavior and improving therapeutic strategies, as conventional culture systems fail to capture the complex interplay of cellular, biochemical, and physical cues present *in vivo*. GBM progression is driven by a heterogeneous TME, where hypoxia, cell–matrix interactions, and stromal crosstalk orchestrate proliferation, invasion, and therapy resistance [18]. To this end, we first carried out a comparative study employing a simplified, yet biologically relevant, static 3D co-culture model, embedding GBM cells and astrocytes, either alone or together, in GelMA and Ch hydrogel droplets selected for their similar mechanical properties and distinct biochemical characteristics. The choice of GelMA and Ch hydrogels was driven by the need to compare the effects of distinct extracellular matrix biochemical cues while minimizing differences in matrix mechanics. GelMA retains collagen-derived bioactive motifs, including RGD sequences that support integrin-mediated cell adhesion [80], whereas Ch is a GAG-mimetic

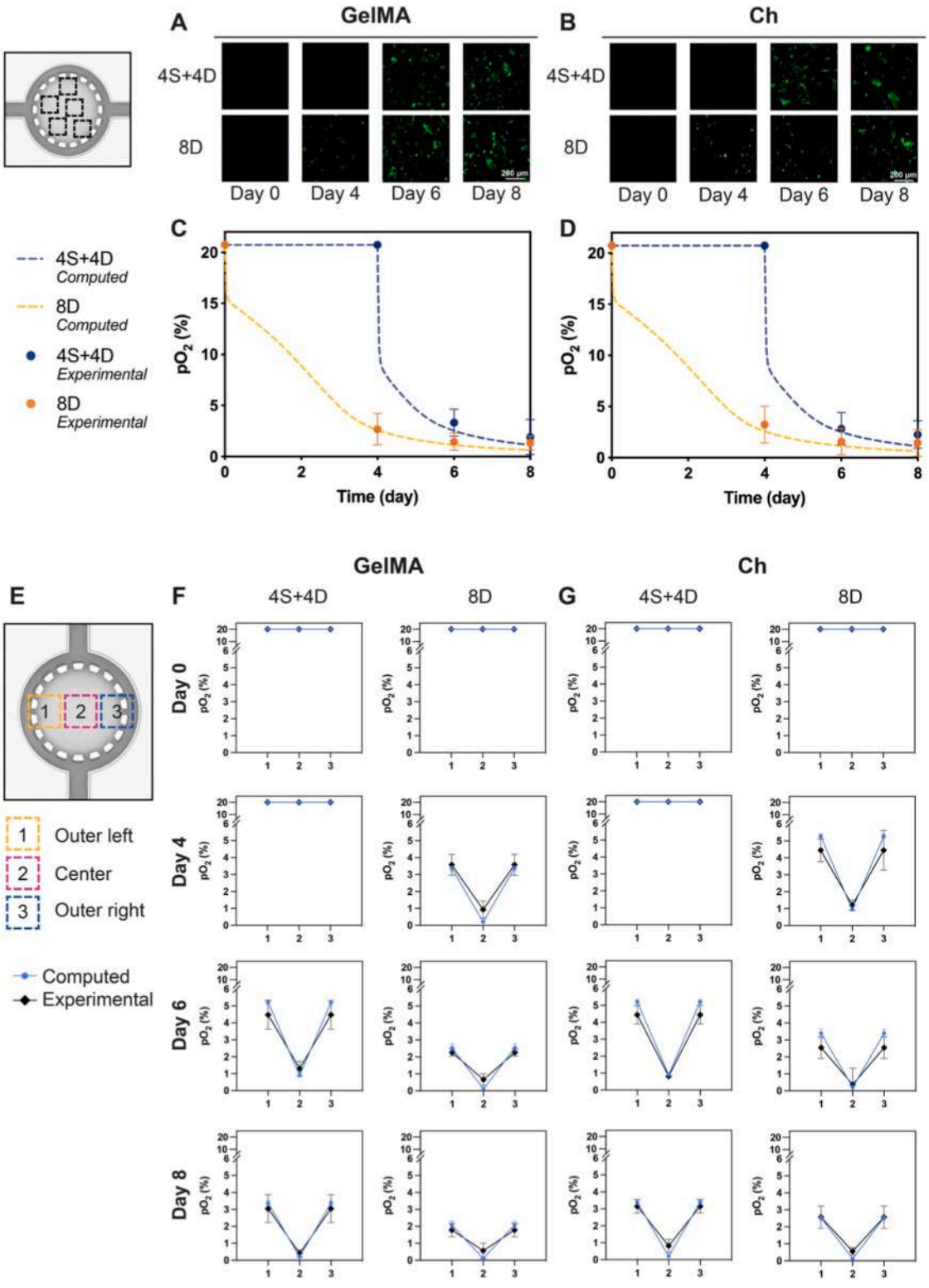

Fig. 8. Experimental validation of computational oxygen predictions through oxygen-sensitive fluorescent probe imaging. A,B) Representative confocal images showing the progressive increase in probe fluorescence during culture in GelMA (A) and Ch (B) hydrogels under the two culture protocols. Five randomly selected fields (dashed squares in the left scheme of the chip) have been acquired. Scale bar 200 μm. C,D) Temporal evolution of oxygen concentration for both GelMA and Ch GBM-on-chip platforms. Experimental measurements (blue and orange dots) obtained from five randomly selected fields within each chip are compared with COMSOL predictions (dashed lines) for both the experimental protocols (4S+4D, 8D). Fluorescent Images were converted into oxygen concentration values using the calibration equations reported in Figure S9 E) Schematic representation of the three analyzed regions used for spatial oxygen quantification (outer left:1, center:2, and outer right:3). Representative fluorescence images are shown in Figure S10 F,G) Spatial oxygen distribution across the microfluidic chips at different culture times for both the experimental protocols (4S+4D, 8D). The graphs compare experimentally measured oxygen concentrations (black) with the pO_2 values predicted by the computational model (blue) in the analyzed regions. Data are presented as the mean ± SD. (For interpretation of the references to color in this figure legend, the reader is referred to the Web version of this article.)

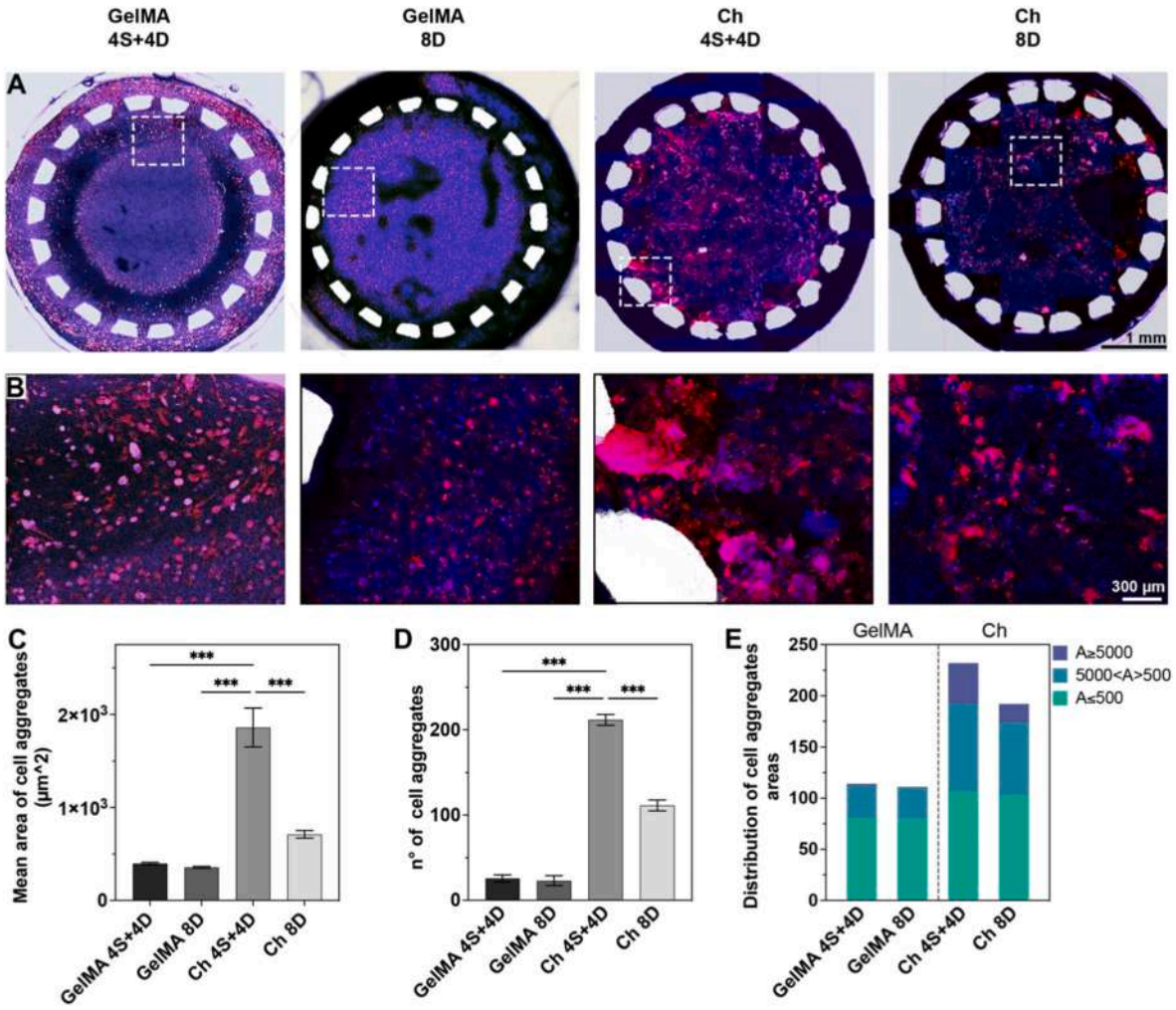

Fig. 9. Morphology of U87-MG and SVG-A cells embedded in hydrogel drops (GelMA or Ch) cultured for 8 days in a GBM-on-Chip system. A continuous flow rate of 100 µL/h was applied either after 4 days of static culture within the chip (4S+4D) or immediately after seeding (8D). A) Overview images showing the central well of the GBM-on-Chip system at the end of the culture period within GelMA (left) or Ch (right) hydrogel (day 8). Scale bar: 1 mm. B) Magnified views of the same samples, indicated by dashed squares in (A). Scale bar: 300 µm. Phalloidin (red) stains the cytoskeleton, DAPI (blue) stains nuclei. Note: the presence of cell aggregates is enhanced in the Ch hydrogel when the fluidic culture starts after 4 days of static culture. Image analysis of (from left to right) mean area (C), number (D), and areas distribution (E), expressed in μm^2 of cell aggregates, performed on fluorescence micrographs (n = 3, images are representative of at least three independent samples). Data are presented as the mean ± SD. (For interpretation of the references to color in this figure legend, the reader is referred to the Web version of this article.)

polysaccharide that shares structural similarities with glycosaminoglycans [81,82], major components of the GBM ECM. First, both GelMA and Ch formulations were subjected to physicochemical characterization. The high long-term stability (up to 15 days under physiological conditions) observed for GelMA and Ch supports the selection of these two materials for a reliable *in vitro* model. A similar resistance to osmotic expansion was observed for the two matrices, as indicated by their comparable swelling behavior. Consistently, the compressive mechanical properties of GelMA and Ch were not significantly different (8.2 ± 1.9 kPa and 6.2 ± 0.7 kPa, respectively). Nevertheless, GelMA and Ch exhibited distinct rheological profiles reflecting their different gelation mechanisms. GelMA undergoes rapid UV-induced covalent crosslinking, leading to a sharp increase in the storage modulus (G′), which remained higher than the loss modulus (G″) during the entire time sweep analysis, indicating a strong elastic dominance [83]. In contrast, Ch displays thermoresponsive gelation driven by physical interactions, as evidenced by the progressive increase in G′ at elevated temperature (37°C). To further characterize the mechanical properties of the two hydrogel formulations, AFM-based force–distance measurements were performed on the hydrogel surface and on cross-sectional slices, enabling comparison of the surface and internal mechanical properties. For both hydrogels, the Young's modulus values obtained by AFM were slightly lower than those measured by bulk compression testing. This discrepancy is likely attributable to the intrinsic differences between the two techniques, including the differences in testing scale, the localized nature of AFM indentation, and the sensitivity of AFM to microscale structural heterogeneities that are averaged in bulk measurements [84,85]. Interestingly, internal measurements revealed no substantial differences in the mechanical properties of the two hydrogel formulations, in agreement with the results obtained from bulk compression tests.

Subsequently, GelMA and Ch were employed to encapsulate a well-established GBM cell line (U87-MG), and an astrocytic cell line (SVG-A), both in mono and co-culture models. U87-MG cells, originally derived from a human malignant glioma, are widely used as an *in vitro* model of GBM due to their robust proliferative capacity, invasive behavior, and expression of key GBM-associated molecular markers [86]. SVG-A cells are immortalized human fetal astrocytes commonly used as a representative model of non-tumorigenic astrocytes in the central nervous system. However, neither cell line fully recapitulates the cellular heterogeneity, molecular and genomic landscape, or functional

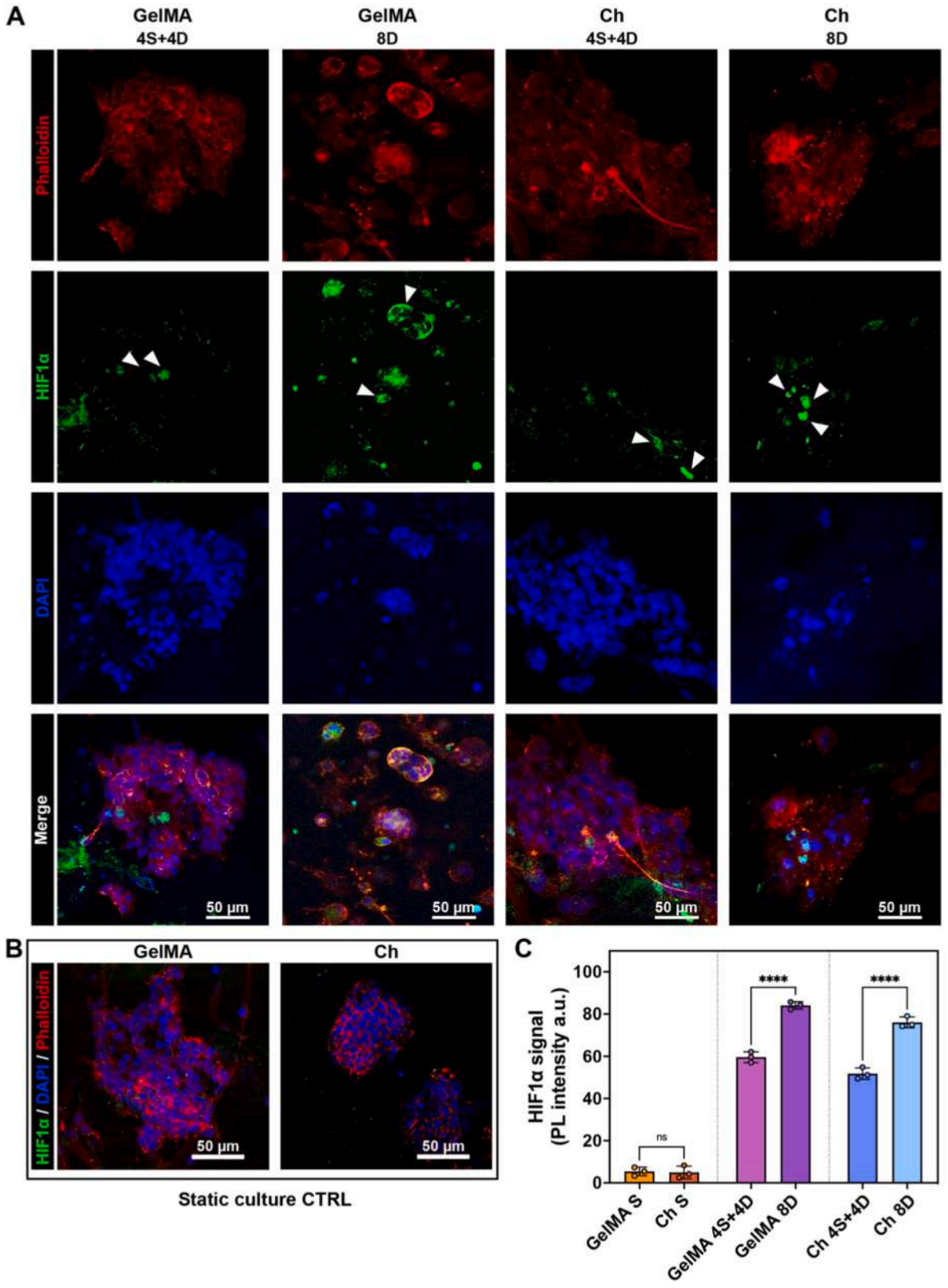

Fig. 10. Hypoxia marker immunostaining in the GBM-on-Chip system. A) Representative immunofluorescence images of U87-MG and SVG-A cells embedded in hydrogel drops (GelMA or Ch) and cultured for 4 days in static conditions and 4 days in dynamic conditions (4S+4D) or 8 days in dynamic conditions (8D), applying a continuous flow rate of 100 µL/h in a GBM-on-Chip system. Cell nuclei were stained with DAPI (blue), cytoskeleton with Phalloidin (red), while HIF1α (green) was used as hypoxia marker. White arrowheads highlight intracellular HIF1α localization. B) The same experiment was performed on U87-MG and SVG-A cells embedded in hydrogel drops of GelMA or Ch cultured for 8 days in static conditions in a multi-well plate. Scale bars: 50 µm. C) Quantification of HIF1α expression based on fluorescence intensity, normalized to the cell-covered area (n = 3). Data are presented as the mean ± SD. Note that under dynamic conditions maintained for 8 days, both GelMA and Ch Organ-on-Chip systems show increased hypoxia-marker expression compared with the other conditions. (For interpretation of the references to color in this figure legend, the reader is referred to the Web version of this article.)

characteristics of primary GBM tumors and adult tumor-associated reactive astrocytes. In particular, reactive astrocytes actively interact with glioma cells and promote tumor progression, invasiveness, and survival through the secretion of a wide range of cytokines and other signaling molecules *in vivo* [87–90]. Therefore, the findings reported in this study should be interpreted within the limits of this model, and future validation in patient-derived GBM cells is mandatory. Nevertheless, the use of established cell lines represents a practical and highly reproducible approach for the biofabrication of *in vitro* tumor models. Within this context, the proposed strategy provides a reliable 3D platform to investigate tumor–astrocyte interactions, enabling the evaluation of cell–cell crosstalk and its influence on GBM behavior in biomimetic hydrogel systems. Both hydrogel formulations demonstrated high biocompatibility, supporting cell survival throughout the culture period. However, optical and electronic microscopy revealed that matrix composition dictates strong differences in cell morphology and spatial organization. GelMA promoted pronounced cell-matrix adhesion and an elongated morphology, particularly for U87-MG cells, while Ch favored spheroid formation for both cell types. The larger spheroids observed in Ch hydrogel compared to GelMA are likely attributable to differences in matrix adhesivity and chemistry. Indeed, GelMA provides cell-adhesive cues that enhance cell–matrix interactions and limit extensive aggregation, whereas the non-adhesive and cationic nature of Ch could promote intercellular interactions, facilitating spheroid growth and coalescence, especially in the co-culture model. Although further investigations are needed to confirm this mechanism, it is likely that this microenvironment allows for increased cellular rearrangement and aggregation, supporting the well-documented reciprocal interactions between GBM cells and astrocytes [91,92], and ultimately leading to the formation of larger spheroids within the Ch matrix. In addition, the higher porosity measured for Ch hydrogel (0.95 ± 0.02) compared to GelMA (0.80 ± 0.03) may contribute to this behavior by providing a more permissive three-dimensional environment for cellular organization and spheroid expansion. This interpretation is further supported by the higher permeability of the Ch hydrogel and its greater rhodamine diffusion compared with GelMA, indicating enhanced molecular transport through the matrix. Improved transport of nutrients, oxygen, and soluble signaling molecules may facilitate cell viability, migration, and intercellular communication, thereby contributing to spheroid growth. Collectively, these findings suggest that both biochemical interactions and the distinct transport properties of the hydrogels contribute to the different spheroid morphologies observed. Notably, spheroids formation occurred directly within the hydrogel matrix, avoiding the need for pre-formed aggregates, and potentially preserving native cell–matrix interactions and spheroid architecture.

These observations were further corroborated under dynamic culture conditions using the *ad-hoc* designed GBM Organ-on-Chip platform, in which GBM cells and astrocytes were exposed to a controlled laminar flow, a biomechanical cue absent in the static model. The pronounced formation of large cell aggregates in Ch, particularly following an initial static phase and subsequent perfusion, suggests that this hydrogel provides a microenvironment capable of stabilizing spheroids even under continuous media flow. This behavior may result from the enhanced retention of cell-secreted factors within the Ch network, limiting their convective removal during perfusion [93]. In contrast, GelMA predominantly supported dispersed cell morphologies under dynamic conditions, which is consistent with the rapid washout of autocrine and paracrine signals within its network [94]. Collectively, these findings suggest that Ch more effectively provides a pro-aggregative tumor microenvironment under perfusion. More importantly, in the GelMA co-culture model, U87-MG cells predominantly organized into a network surrounding SVG-A spheroids, whereas in the Ch-based co-culture model, U87-MG and SVG-A cells exhibited extensive cell–cell interactions, forming mixed spheroids composed of both cell populations. These results suggest the ability of Ch to promote GBM-like multicellular organization and its potential suitability for modeling tumor spheroid formation in microfluidic systems.

At the same time, both matrices only marginally support cell-mediated ECM remodeling—photocrosslinked GelMA remains structurally stable over culture periods comparable to ours despite its MMP-sensitive motifs [95], and chitosan is poorly degraded by mammalian cells, which lack endogenous chitosanases [82]—meaning that the dynamic ECM remodeling of the GBM microenvironment is only partially recapitulated and remains to be addressed in future long-term studies.

Currently, Organ-on-Chip devices are mostly fabricated in PDMS by soft-lithography technique, a process that is time-consuming, costly, and poorly scalable [96,97]. With the aim of speeding the prototyping process and providing an easy customization, other than lowering the production costs, in this study we fabricated our microfluidic platform by 3D printing DLP technology, one of the currently most explored OoC fabrication methods [98]. By means of DLP technique, we rapidly prototyped the GBM-on-Chip with a transparent and biocompatible resin, ensuring a level of resolution adequate for our cell culture studies [99]. In addition, we developed a computational model of the microfluidic system that incorporates both fluid dynamics and oxygen transport coupled to cellular consumption. As a matter of fact, *in silico* approaches complement experimental studies [100,101] by enabling systematic exploration of the design space [102], rapid hypothesis testing and integration of heterogeneous data into a coherent theoretical framework [103,104]. Our *in silico* approach enabled us to assess key parameters, such as flow velocity, diffusion-driven transport inside the hydrogel, and spatiotemporal oxygen distributions, that are challenging to measure directly through experimental techniques [100–103,105]. Some simplifications nonetheless remain and should be considered when interpreting the results. The model describes oxygen transport at the construct scale, assuming a homogeneous cell distribution and time-invariant hydrogel properties, while local microgradients and dynamic matrix remodeling are not explicitly resolved. Furthermore, cell-specific metabolic variations were not included, and the predicted pO_2 values should therefore be interpreted as an approximation of the overall oxygenation state of the construct rather than the evolving pericellular microenvironment. A detailed description of the assumptions and limitations underlying the oxygen transport model is provided in Appendix 1 of the Supplementary Information.

However, a major strength of the present study is the direct experimental validation of the computational predictions through quantitative oxygen mapping. By calibrating an oxygen-sensitive fluorescent probe under controlled oxygen conditions, fluorescence measurements acquired within the GBM-on-Chip were converted into local oxygen concentrations and directly compared with the simulated pO_2 profiles. The agreement between experimental and computational data demonstrates that the model accurately predicts both the temporal evolution and spatial distribution of oxygen within the microfluidic platform. This validation substantially increases the reliability of the computational framework and supports its use as a predictive tool for designing and optimizing hypoxic microenvironments in Organ-on-Chip systems.

Modeling hypoxia is especially critical in GBM research, as low-oxygen regions drive malignant traits, including altered metabolism, invasion, therapy resistance, and maintenance of treatment-resistant cell states [56,63,66,106,107]. Previous studies employing microfluidic systems have demonstrated that controlled oxygen gradients can be established and maintained on chip, producing spatially heterogeneous hypoxic signaling that more faithfully replicates *in vivo* conditions than standard normoxic cultures [108–111], yet quantitative experimental validation of computational oxygen transport models remains relatively uncommon. By combining experimentally measured oxygen levels with numerical simulations, our approach provides a robust framework for accurately characterizing hypoxia within the GBM-on-Chip platform. Importantly, while quantitative oxygen mapping validated the computational model, HIF1α expression independently confirmed that the predicted hypoxic microenvironment elicited the expected cellular response, thereby linking the physical

characterization of oxygen availability with its biological consequences. Furthermore, our results demonstrate the versatility of the proposed platform, showing that both spheroid growth and the extent of the hypoxic window can be modulated by adjusting the culture protocol. The progressive establishment of a stable hypoxic microenvironment in our device is consistent with chronic hypoxia, which characterizes diffusion-limited and peri-necrotic regions of GBM and is associated with sustained HIF signaling, metabolic reprogramming, enhanced invasiveness, stem-like phenotypes, and therapeutic resistance. In contrast, cycling hypoxia, generated by transient fluctuations in tumor perfusion and oxygen delivery, induces repeated hypoxia–reoxygenation episodes that promote oxidative stress, inflammatory signaling, and dynamic regulation of hypoxia-responsive pathways [59,112–114]. While the current platform is designed to reproduce chronic hypoxia rather than temporal oxygen oscillations, future iterations could incorporate programmable modulation of perfusion conditions, for example through controlled variation of the flow rate, to generate temporal changes in oxygen availability and thereby emulate aspects of cycling hypoxia. By integrating computational prediction with experimental validation, this platform provides a controlled system to investigate hypoxia-driven GBM behaviors under physiologically relevant oxygen conditions, while offering the potential to explore more dynamic oxygen environments in future implementations.

Although the complexity of GBM hypoxia *in vivo*, which involves abnormal vasculature, immune infiltration, metabolic gradients, necrosis, and dynamic oxygen fluctuations [115], is not fully reproduced in this chip, the model successfully recapitulates several key features of the TME, including a 3D ECM, heterotypic cell-cell interaction between U87-MG and SVG-A, and clinically relevant hypoxia. Moreover, the modular design of the platform makes it readily adaptable for higher-throughput drug screening. This scalability is enabled by the DLP 3D-printing approach, which allows rapid fabrication of customized and parallelized architectures directly from CAD designs without additional tooling.

By integrating experimental validation and computational prediction, the platform provides a powerful tool to optimize device geometry, culture protocols, and perfusion conditions, supporting the rational design of physiologically relevant hypoxic microenvironments. Although the current platform incorporates tumor and astroglial cells, it does not yet include other key cellular component of the GBM microenvironment, such as microglia, macrophages, endothelial cells, pericytes, or neurons, which are known to influence tumor progression and hypoxia responses [114,116]. Nevertheless, the modular architecture of the device provides a flexible framework for the future incorporation of these additional cell populations, enabling more biomimetic modeling of the GBM TME. This platform may contribute to the future development of precision medicine approaches by providing a controlled and physiologically relevant system for evaluating GBM cellular responses and therapeutic effects under biomimetic microenvironmental conditions.

4. Methods

4.1. GelMA hydrogel preparation

10 g of gelatin from porcine skin (type A, ~175 bloom, G2625, Sigma Aldrich, Milan, Italy) was dissolved in 100 mL of PBS at 50°C in an oil bath under stirring, to get a final concentration of 10% (w/V). Once the gelatin solution was clear, 0.7 mL of methacrylic anhydride (MA) (Sigma Aldrich) were added dropwise, to get a degree of substitution (DS) of 50 ± 8%. The resulting solution was left under stirring at 50°C for 3 h. The methacrylation process was then stopped diluting with 400 mL PBS. The solution was then transferred in pre-soaked dialysis membranes (Spectro/Por molecular porous membrane tubes, MWCO 12-14 kDa, #08-801-244, Fisher Scientific, Milan, Italy), to dialyze the GelMA solution against deionized water for 7-8 days at 40°C (changing water twice daily), to remove unreacted methacrylic anhydride and methacrylic acid. At the end of the dialysis the GelMA solution was transferred to 50 mL Falcon tubes, frozen at −80°C overnight, and then lyophilized for 72 h. The lyophilized GelMA was dissolved in a pre-warmed PBS, containing 10% w/V of FBS (Life Technologies), to obtain a 10% (w/v) GelMA solution. The solution was stirred at 50°C until complete dissolution, and then 0.5% w/v of LAP (Lithium phenyl-2,4,6-trimethylbenzoylphosphinate, Sigma Aldrich) was added and let react for 1 h at 50°C under stirring in the dark. The resulting GelMA hydrogel was used for further experiments.

4.2. Ch hydrogel preparation

Low molecular weight chitosan (Sigma Aldrich) was used for hydrogel preparation. The hydrogel was prepared starting from a 3.33% (w/v) solution of chitosan (Ch) in 0.1 M HCl (Sigma Aldrich). The solution was kept under stirring at room temperature overnight. The gelling agent (GA) solution was prepared by dissolving β-glycerophosphate powder in MilliQ water to a final concentration of 0.5 M. The hydrogel was prepared by cold mixing the chitosan solution with the GA in a 3:2 ratio.

4.3. Swelling test

The swelling ratio is the fractional increase in the weight of the hydrogel due to water absorption and is useful to determine the amount of media that could be retained by the hydrogel network. Cylindrical structures (Ø ≃ 8 mm, h ≃ 5 mm) from GelMA and Ch solutions have been obtained from a PDMS mold, immersed in PBS at 37°C, and weighted at different time points for 24h. The swelling ratio (SR) percentage is calculated as:

$$SR(\%) = \left[\frac{W\text{wet} - W\text{dry}}{W\text{dry}}\right] \times 100 \quad (1)$$

Where W_{dry} is the weight of sample at time 0 and W_{wet} is the weight of the hydrated sample.

4.4. Stability test

The hydrogel stability test is used to determine the stability of the material in physiological conditions in a non-enzymatic environment. The hydrogel was immersed in PBS at 37°C and its weight was measured at different time points over 15 days. The weight variation of the material was calculated as:

$$Weight\ variation(\%) = \left[\frac{Wi - Wd}{Wd}\right] \times 100 \quad (2)$$

Where W_i is the initial weight and W_d is the weight that is measured at different time points.

4.5. Compression test

Swollen GelMA and Ch samples after the swelling tests were measured with a gauge to determine diameter and thickness and then tested with a Z5.0 testing machine (Zwick/Roell, Germany), equipped with a 10 N load cell to determine the hydrogels stiffness. The test was performed at room temperature, up to 75% deformation and with a displacement velocity of 2 mm/min [117], obtaining the compressive stress–strain curves. At least 3 samples were measured for both hydrogels. The Young's modulus was calculated as the slope of the linear part of the stress–strain curve between 1% and 5% of the strain and plotted.

4.6. Rheological properties

The rheological properties of GelMA and Ch solutions were tested by

a rheometer (MCR 301, Anton Paar Physica) equipped with a 25-mm cone-plate geometry. Temperature-sweep tests were performed on Ch at 22°C and 37°C with a frequency of 1 Hz and a strain of 10%. To investigate the effect of photopolymerization on GelMA rheological properties, time-sweep measurements were performed at room temperature at a frequency of 1 Hz and a strain of 3% in the rheometer connected with Omnicure LX500 UV LED Spot Curing system (385 nm). UV exposure time was 60 s for all samples with a 1.1 W/cm^2 irradiance.

4.7. AFM force-distance characterization

Force–distance measurements were conducted in liquid at room temperature after soaking both the hydrogel cylinders and the corresponding cross-sectional slices in PBS for 24 h. The analysis was performed using a JPK NanoWizard V Atomic Force Microscope (Bruker, Germany) equipped with a SAA-SPH-1UM cantilever (Bruker) featuring a cylindrical tip with a hemispherical end of 1 μm radius (spring constant: 0.25 N/m). Young's modulus maps were acquired using the Quantitative Imaging (QI™) advanced mode, in which a complete force–distance curve was recorded at each pixel by indenting the sample surface until a predefined force threshold was reached. A setpoint force of 1 nN and a z-range of 4000 nm were applied, and at least three maps (5 × 5 μm^2, 112×112 pixels) were collected for each sample. Young's modulus values were obtained by fitting each force–distance curve pixel by pixel using the Hertz contact model, as implemented in the JPK analysis software [85,118].

4.8. Cell culture and cell encapsulation within the hydrogels

The U87-MG human glioblastoma and SVG-A human astrocyte cell lines were cultured in Dulbecco's Modified Eagle Medium (DMEM, Life Technologies) supplemented with 10% FBS, in the presence of 100 U/mL of Na-penicillin and 100 μg/mL of streptomycin sulfate purchased from ECACC (European Collection of Authenticated Cell Cultures, Salisbury, UK), whereas the SVG-A astrocyte cells were obtained from R.S. Lahue Laboratory, Human Molecular Genetics Lab, University of Galway, Ireland [119]. Cells were cultured at 37°C with 95% humidity and 5% CO_2. After preliminary tests, a cell density of 1 million cells per mL of hydrogel was chosen for cell encapsulation, by gently mixing the cells, resuspended in 50 μL of medium, within the hydrogel solution. Drops (40 μL) of cell-laden Ch hydrogel were placed in a 24-well cell culture plate and then incubated at 37°C to induce the sol–gel transition of the thermo-responsive hydrogel. After 10 min, complete DMEM was added to each well. Alternatively, drops (40 μL) of cell-laden GelMA hydrogel were placed in a 24-well cell culture plate and immediately exposed to UV irradiation for 60 s to induce hydrogel crosslinking. Samples were then incubated at 37°C with 95% humidity and 5% CO_2 for 20 min for further experiments. U87-MG and SVG-A cells have been embedded in hydrogel drops generating a mono-culture model (with U87-MG or SVG-A cells) or a co-culture model in which both the cell types were used together.

4.9. Live/dead staining of cells encapsulated within the hydrogels

The live/dead assay was performed to evaluate cell viability inside the GelMA and the Ch hydrogels. The cell-encapsulated hydrogel drops were incubated with a working solution, composed by NucBlue® Live reagent (ReadyProbes® Cell Viability Imaging Kit) or Calcein-AM (Invitrogen) and propidium iodide in pre-warmed DMEM, depending on the experiments. The working solution was left reacting for 1 h in the dark and then removed. Fluorescent images were obtained using an inverted fluorescence microscope (Evos M7000, Thermo Fisher), with specific wavelengths following manufacturer's instructions.

4.10. Presto Blue assay

Presto Blue assay (Invitrogen) was performed at days 1, 3, and 7 of cultivation of the cell-laden hydrogel drops, to evaluate the metabolism of the cells encapsulated in the hydrogels, according to the manufacturer's instructions. Briefly, the samples were deprived of culture medium and incubated at 37°C for 2 h in the dark in the presence of the Presto Blue reagent. At the end of the incubation time, the medium was recovered and the absorbance at 570 nm was read using a spectrophotometer. Data were expressed as a percentage of metabolic activity, and all the results were normalized to day-1 values.

4.11. Scanning electron microscopy (SEM) analysis

Drops of GelMA and Ch hydrogels with encapsulated cells (U87-MG, SVG-A, U87-MG + SVG-A) were cultured for 8 days, and analyzed using scanning electron microscopy (SEM EVO 40, Carl Zeiss AG). After cultivation, samples were washed twice with 1× PBS, fixed with 4% paraformaldehyde solution (PFA) for 10 min at room temperature, and finally washed with 1× PBS. The samples were then dehydrated in increasing concentrations of ethanol (50%, 70%, 95% and 100%) and left to dry overnight. Prior to SEM imaging, samples were coated with a 10-nm gold layer by sputtering (CCU-010 HV, Safematic GmbH). Images at 2-3k× magnifications were acquired with an accelerating voltage of 5 kV.

4.12. Generation of GFP-U87-MG and TOMATO-SVG-A fluorescent cells

2.5 × 10^6 subconfluent U87-MG cells were stable transfected by electroporation with Neon Transfection System (Invitrogen) at 1300 V, 30 ms, in the presence of 30 μg of pEGFP-N1 vector (Real Gene Biotech Company), encoding green fluorescence protein (GFP) in 3 mL DMEM. Cells were subsequently diluted to 10 mL DMEM without FBS and antibiotics and seeded in a 10-cm culture dish, with medium replacement after 6 h. Antibiotic selection of transfected cells was performed with the neomycin analogue G418 (Sigma), added at 0.8 mg/mL 48 h after the transfection and replaced twice a week. The pool of U87-MG neomycin resistant cells was used for experiments.

Stable transfection of 2.5 × 10^6 subconfluent SVG-A human astrocyte cells was performed by 60 μL of Transfectin Reagent (Biorad) in the presence of 30 μg of ptdTomato-N1 vector (Clontech), encoding tdTomato, a member of the family of fruit fluorescent proteins derived from the *Discosoma sp* [51], Red fluorescent protein, DsRed, in 3 mL of DMEM without FBS and antibiotics, and plated in a 10-cm dish. The medium was replaced after 6 h. The neomycin analogue G418 (Sigma) was added at 0.8 mg/mL 48 h after the transfection and the medium was changed twice a week. The pool of SVG-A transfected and neomycin resistant cells were used for experiments. The percentage of positive cells was evaluated by acquiring several fluorescence and bright-field micrographs of U87-MG and SVG-A cells and calculating the ratio of fluorescent to total cells. Both cell lines were approximately 70% transfected.

4.13. Live-cell imaging of transfected GFP-U87-MG and TOMATO-SVG-A cells

For the evaluation of cell aggregates growth, the cells-laden hydrogel drops obtained from transfected GFP-U87-MG and TOMATO-SVG-A cells were cultured for 8 days as previously described. Fluorescence and bright-field micrographs of the entire drops were automatically acquired every 24 h for 8 days with an inverted fluorescence microscope (Evos M7000, Thermo Fisher). The number and area of cell aggregates were analyzed using the ImageJ software and visualized with GraphPad Prism v.10. Quantification was performed on spheroids obtained from three independent experiments (n = 3), demonstrating reproducible spontaneous spheroid formation despite the expected biological

heterogeneity in spheroid size. To further assess the reproducibility of spheroid formation, the coefficient of variation (CV) of the mean spheroid area was calculated as the ratio of the standard deviation (SD) to the mean of the three experimental replicates, expressed as a percentage according to the following equation:

$$CV(\%) = \left(\frac{SD}{mean}\right) \times 100 \quad 3$$

4.14. Chip design and fabrication

The microfluidic device, used to construct the GBM-on-chip, has been designed using Rhinoceros Software (Robert McNeel & Associates, v6.0) (Fig. 6A, Fig. S4). The chip consists of a central microchannel with a width of 1 mm and a height of 1.5 mm. The channel crosses a central well, with a radius of 3.5 mm, which will host the cell-laden hydrogel inside an inner space, surrounded and delimited by a pillars' crown with an inner radius of 2.5 mm. The inlet and outlet of the chip are symmetrically positioned and consist of integrated connectors, useful for the tube insertion and microfluidic set-up (Fig. S5). The chip is fabricated using Digital Light Processing (DLP) 3D-Printing technology (Asiga MAX X27 UV 3D printer, Asiga, Australia), with a printable volume of 51.8 mm × 29.2 mm × 75 mm and a *xy* resolution of 27 μm, equipped with a high power led (385 nm). A biocompatible resin (GR-10 resin, pro3dure medical GmbH, Germany) was chosen as chip fabrication material [99]. The printing parameters were experimentally optimized to ensure dimensional accuracy and structural integrity (Table S1). Once printed, the chip undergoes a cleaning phase with 2-propanol (IPA) to remove excess resin, and it is placed under UV light (30 min each side) to further polymerize the resin and obtain the final cured device. The device is then assembled and closed by a transparent polystyrene (PS) cover, fabricated by CNC micromilling (Mini-mill3 NSK E3000 from MiniTech Machinery, Norccross, GA, USA). The PS cover was fixed using 6 screws and 6 nuts, positioned on the long sides of the device. To ensure a hermetic seal of the device, a 300 μm-thick Polydimethylsiloxane (PDMS) membrane (Sylgard 184, base-to-curing-agent ratio 10:1, fabricated by spin-coating on a silicon wafer at 700 rpm for 45 s) was oxygen-plasma bonded to the PS cover.

4.15. Computational simulation setup

The computational models were carried out using COMSOL Multiphysics (COMSOL Inc., version 6.1, 2023, Stockholm, Sweden), a finite element software particularly suited for multiphysics simulations. In microfluidic devices with small geometric length scales, fluid motion is governed by the continuity and the Navier–Stokes equations [120]. To determine the appropriate flow regime for our chip, the Reynolds number (Re) was calculated as:

$$\Re = \frac{\rho U D}{\mu} \quad 4$$

Where ρ is the fluid density, U the velocity, D the characteristic length and μ the dynamic viscosity. Water was selected as the reference fluid in this study, which is a popular choice for *in silico* simulations of biomicrofluidic chips [121–123], as it is a Newtonian fluid, and its rheological properties reasonably approximate those of DMEM through the chip in the experimental study [124]. Using water density and viscosity values adjusted for 37°C (cell culture conditions), with a characteristic length of 3.5 mm and an inlet flow rate of 100 μL/h, the Reynolds number was estimated to be approximately 0.34 which corresponds to laminar regime. This was expected, since in the microfluidic realm, flow is generally laminar, with viscous forces overcoming inertial ones [105, 125]. No-slip boundary conditions were imposed on the walls, while a fully developed flow was applied at the inlet and a zero-gauge pressure condition at the outlet (Fig. 6B). To account for the porous nature of the Ch and GelMA hydrogels, a Darcian flow [126] was implemented within the hydrogel domain (Fig. 6B). The hydraulic permeability of the GelMA and Ch formulations was measured experimentally following the approach of Gao et al. [127], using a purpose-built permeability setup in which GelMA and Ch were cast. Each hydrogel was perfused with MilliQ water using an Elveflow OB1 MK3+ pressure controller (Elveflow, Paris, France) coupled with an inline flow sensor, varying the applied pressure between 200 and 2000 mbar while recording the steady-state volumetric flow rate Q. Within the tested range, Q varied linearly with the applied pressure ΔP ($R^2 > 0.999$; Fig. S6), confirming that the measurements lay within the linear Darcy regime, from which the hydrogel permeability was obtained as:

$$\kappa = \frac{\mu Q L}{A \Delta P} \quad 5$$

Where L is the hydrogel height (fixed at $L = 1.5$ mm), A is the hydrogel surface area (fixed at $A = 50.27$ mm^2), and μ the water dynamic viscosity at 25°C (fixed at 0.89 mPa × s). After accounting for the hydraulic resistance of the empty setup, the measured values were $\kappa = (4.1 \pm 0.6) \times 10^{-16}$ m^2 for GelMA and $\kappa = (1.2 \pm 0.4) \times 10^{-14}$ m^2 for Ch.

Hydrogels porosity was experimentally determined as the ratio between the pore volume and the total volume of the fully swollen hydrogel (n = 3). The pore volume was assumed to correspond to the amount of water retained under equilibrium swelling conditions, with complete saturation and full pore occupancy. To calculate this, the volume of the dry polymer network, obtained after freeze-drying, was subtracted from the total swollen volume. The total volume was defined as the volume of the hydrogel in its fully hydrated state, including both the polymer matrix and the absorbed water. Porosity was then calculated using the following formula:

$$\frac{Pore\ V}{Total\ V} = \frac{Total\ V - Dry\ polymer\ V}{Total\ V} \quad 6$$

The porosity, as determined by the described method, resulted to be 0.80 ± 0.03 for GelMA and 0.95 ± 0.02 for Ch. Finally, a physics-controlled mesh was selected using the in-house COMSOL mesh builder, and the grid independence of the result was checked by globally refining the mesh to obtain finer tetrahedra throughout the domain. A total of 2,190,485 tetrahedral elements provided mesh-independent results (Fig. 6B).

4.16. Diffusion model validation

The diffusion model was validated experimentally under acellular conditions. Fresh GelMA and Ch hydrogels were cast in the chip well and the device was perfused at 100 μL/h with a rhodamine 6G solution (0.1 mg/mL). Dye penetration into the hydrogel was recorded over 250 min by fluorescence microscopy and expressed as normalized concentration. Fluorescence imaging was performed using an EVOS M7000 Imaging System (Thermo Fisher) equipped with an Olympus 4× apochromatic objective (AMEP4904; NA = 0.16, WD = 13 mm). Rhodamine 6G fluorescence was acquired using the EVOS RFP light cube. Automated tile scanning was performed to acquire multiple overlapping fields of view covering the entire central chamber of the microfluidic chip, and the acquired images were stitched to generate a complete fluorescence mosaic reconstruction using the integrated EVOS M7000 Software (Thermo Fisher). The same experiment was reproduced *in silico* by solving a time-dependent convection–diffusion problem coupled with the laminar-flow and Darcy velocity field described in the previous subsection. The computed concentration maps and temporal profiles were compared with the experimental ones (Fig. 6E–H). The free-diffusion coefficient of rhodamine in water was set to 4.14×10^{-10} m^2/s [128]. Matrix-specific values were assigned as follows: for GelMA, a value of 4×10^{-11} m^2/s, reported for rhodamine 6G in a gelatin-based hydrogel by fluorescence correlation spectroscopy [77]; for Ch, a value of 2.3×10^{-10} m^2/s, obtained by scaling the free-water coefficient through an obstruction factor derived from

proton-NMR measurements of small-molecule diffusion in chitosan gels of comparable polymer content [78], due to lack of literature data for rhodamine in Ch. Model agreement was quantified by the coefficient of determination (R^2) between computed and experimental normalized-concentration time courses (Fig. 6F–H).

4.17. Oxygen transport and consumption simulation

To predict hypoxia development within the chip, an oxygen transport and consumption model was coupled with the laminar flow simulation (Table S2). To account for oxygen diffusion from the external atmosphere through the PS cover and PDMS membrane when the chip is closed, both layers were explicitly included in COMSOL with their actual dimensions: two parallelepipeds of 37 × 25 mm, with a thickness of 2 mm for the PS layer, and 300 μm for PDMS membrane. At 37°C, the diffusion coefficients of oxygen were set to 3.8×10^{-9} m^2/s in aqueous solution [129], 4.1×10^{-9} m^2/s in PDMS [108,130], and 2.3×10^{-11} m^2/s in PS [108,131]. Cellular oxygen uptake reaction was described by Michaelis-Menten kinetics [132,133]:

$$R_{O_2} = (q_{U87-MG}\rho_{U87-MG} + q_{SVG-A}\rho_{SVG-A})\frac{c_{O_2}}{c_{O_2} + k_{MM,O_2}}\delta(c_{O_2} > c_{crit}) \quad 7$$

Here, q is the single-cell oxygen consumption rate, set to 0.005 pmol/min for U87-MG cells [134] and 0.0013 pmol/min for SVG-A cells [135], ρ_{cells} is the cell density, experimentally set to an initial value of 0.5×10^6 cells/mL for both cell cultures. Furthermore, k_{MM,O_2} is the Michaelis-Menten constant for the oxygen – set to 3×10^{-3} mol/m^3 [79] – and c_{O_2} is the local oxygen concentration in time and space, computed by the solver at each step. To avoid overestimating oxygen consumption due to non-viable cells, a Heaviside function δ was introduced so that consumption ceased below a critical oxygen concentration. This critical concentration c_{crit} for hypoxia-induced cell death was set to 1×10^{-4} mol/m^3 [129,136]. The initial oxygen concentration was set to 0.192 mol/m^3 – corresponding to the solubility of oxygen in DMEM at 37°C [137] – within all the chip, assuming complete perfusion of the culture medium at t = 0. The same oxygen concentration was imposed at the inlet throughout the simulation to represent continuous perfusion from the connected syringe pump. Moreover, to account for oxygen transfer from the external atmosphere, the same oxygen concentration boundary condition was prescribed on the PDMS and PS surfaces exposed to air. Although oxygen solubility in PDMS is substantially higher than in the culture medium, the same oxygen concentration was imposed at all air-exposed boundaries to avoid artificial concentration jumps at material interfaces. The resulting differences in oxygen levels are therefore determined by diffusion and material properties within the simulated domains rather than by boundary discontinuities. Regarding the 4S+4D protocol, the simulations describe the perfused phase of the culture protocol, which begins at day 4. The oxygen concentration within the hydrogel at the start of this phase was prescribed as uniform and equal to the concentration of oxygen dissolved in culture medium at equilibrium with the surrounding atmosphere, 0.192 mol/m^3 [137], corresponding to the open, static configuration in which the device is immersed in culture medium within a dish during the preceding four days. The initial cell density for the perfused phase was not predicted by the model but was derived from experimental measurements performed at day 4, resulting in a value of 1.1×10^6 cells/mL for both hydrogels. To account for cellular growth and death, a logistic equation which was implemented through the ordinary differential equation (ODE) interface in COMSOL [79,137]:

$$\frac{d\rho_{cell}}{dt} = u_{max}\frac{c_{O_2}}{c_{O_2} + K_P}\left(1 - \frac{\rho_{cell}}{\rho_{cell,max}}\right)\rho_{cell} - \lambda_{death}\left(1 - \frac{c_{O_2}}{K_{death} + c_{O_2}}\right)\rho_{cell} \quad 8$$

where u_{max} is the maximum proliferation rate under normoxia, K_P is the half-saturation constant for proliferation, $\rho_{cell,max}$ is the maximum achievable cell density within the hydrogel due to space or nutrient limitations, λ_{death} is the maximum death rate under severe hypoxia, and K_{death} is the oxygen concentration at which the death rate is halved. For U87-MG, u_{max} was experimentally estimated from static culture growth over 8 days, obtaining 5.32×10^{-6} 1/s, consistent with literature values [79]. K_P was set to 0.02 mol/m^3 [138], $\rho_{cell,max}$ to 1×10^8 1/mL [79,139], λ_{death} to 5.88×10^{-6} 1/s [79,140] and K_{death} equal to 0.845 $mmol/m^3$ [79,141]. The same parameter set was used for SVG-A cells due to the lack of specific modeling data for this cell line.

4.18. 3D culture in the microfluidic chip

A cell density of 1 million cells per mL of hydrogel was chosen for cell encapsulation in the microfluidic chip, by gently mixing the cells (U87-MG and SVG-A) with the hydrogel solution. A drop (40 μL) of cell-laden Ch hydrogel was dispensed into the central well of the chip, surrounded and delimited by a pillars' crown and then incubated at 37°C in order to induce the sol–gel transition of the thermoresponsive hydrogel. Alternatively, a drop (40 μL) of cell-laden GelMA hydrogel was dispensed into the central well of the chip as previously described and exposed to UV for 60 s to induce hydrogel crosslinking. The chips were hermetically sealed with a transparent PS cover secured by six screws and six nuts, and subjected to dynamic culture conditions for 8 days—either immediately after seeding or starting on day 4—*via* connection to a syringe pump system operating at a flow rate of 100 μL/h.

4.19. Experimental oxygen quantification using an oxygen-sensitive fluorescent probe

To experimentally quantify oxygen concentration within the GBM-on-Chip platform, an oxygen-sensitive fluorescent probe (Image-iT™ Green Hypoxia Reagent, Thermo Fisher Scientific) was employed. This live-cell permeable compound exhibits increased fluorescence under hypoxic conditions due to oxygen-dependent intracellular activation. The fluorogenic response is negligible under normoxic conditions, while provides a hypoxia-dependent fluorescent signal when oxygen level reaches 5%, and progressively increases as oxygen availability decreases, as reported by the manufacturer. To convert fluorescence intensity into oxygen concentration, a calibration procedure was first established using cell-laden GelMA and chitosan hydrogel drops prepared under the same experimental conditions as the GBM-on-Chip constructs. Samples were incubated with 5 μM Image-iT™ Green Hypoxia Reagent for 2 h at 37°C and imaged using a Zeiss LSM980 confocal microscope with a LD Plan-Neofluar 20×/0.4 Korr M27 air objective, equipped with a PeCon live-cell environmental chamber (PeCon GmbH, Germany), allowing controlled regulation of temperature, CO_2, and oxygen concentration throughout the calibration experiments. Samples were sequentially equilibrated at predefined oxygen concentrations spanning normoxic to severe hypoxic conditions (20%, 5%, 2.5% and 0.1% pO_2), while maintaining identical acquisition parameters (laser power, detector gain, pinhole, and offset) throughout the entire calibration procedure. Confocal z-stacks were acquired for each oxygen concentration and converted into maximum intensity projections to include fluorescent cells distributed throughout the entire thickness of the hydrogel. Fluorescence intensity was quantified in Fiji (version 1.54p) as the mean gray value after thresholding to selectively identify fluorescent cells. Under normoxic conditions (21% pO_2), the probe fluorescence remained at background levels and was quantified as zero after thresholding. Increasing fluorescence intensities were detected under hypoxic conditions, with progressively higher signal at decreasing oxygen concentrations. Separate calibration curves were generated for GelMA and Ch hydrogels by linear regression analysis in GraphPad Prism v.10, yielding hydrogel-specific equations relating fluorescence intensity to oxygen concentration (Supplementary Fig. S9). These equations were subsequently used to estimate oxygen concentration from fluorescence images acquired in the GBM-on-Chip experiments.

Prior to imaging, microfluidic chips were perfused with culture medium supplemented with 5 μM Image-iT™ Green Hypoxia Reagent for 4 h to allow probe administration. For temporal oxygen quantification, confocal images were acquired from five randomly selected fields of view within each chip at the different culture time points. Mean fluorescence intensity was converted into oxygen concentration using the corresponding calibration equation and compared with the oxygen consumption predicted by the computational model. For spatial oxygen quantification, fluorescence images were acquired from three predefined regions of the microfluidic device distributed along the hydrogel compartment, including two peripheral regions (Regions 1 and 3) and one central region (Region 2), as illustrated in Fig. 8E. At least three fields per region were acquired. Mean fluorescence intensity was converted into oxygen concentration using the corresponding calibration equation and compared with the spatial oxygen distributions predicted by the computational model considering a specific cut line encompassing the three predefined regions of the microfluidic device. Day 0 in the 8D protocol and days 0 and 4 in the 4S+4D protocol were considered normoxic reference conditions (21% pO_2), as the devices remained in equilibrium with the incubator atmosphere during these culture phases.

To quantify the agreement between the computational predictions and the experimental measurements the root mean square error (RMSE) was quantified as:

$$RMSE = \sqrt{\frac{1}{n}\sum_{i=1}^{n}(S_i - E_i)^2} \quad (9)$$

where S_i and E_i represent the simulated and experimental values, respectively, and n is the total number of paired observations.

4.20. Morphological analysis of embedded cells by DAPI/Phalloidin staining

To evaluate cell morphology and distribution of U87-MG and SVG-A cells within the GelMA and Ch hydrogels, samples were subjected to DAPI/Phalloidin staining. After 8 days of culture the cells-containing hydrogel drops (both in static and dynamic experiments) were washed twice with PBS, fixed with 4% paraformaldehyde (PFA), and permeabilized in 0.2% PBS/Triton X-100 for 15 min. Blocking solution (2% BSA in 0.1% PBS/Triton) was added for 1 h at room temperature. TRITC-Phalloidin (1:1000 v/v in blocking solution) was added to the samples for 20 min at room temperature. Cells nuclei were stained with DAPI. Fluorescent images were obtained by a Carl Zeiss confocal microscope (LSM700) using an EC Plan-Neofluar 40X/1.3 oil-immersion objective.

4.21. Immunofluorescence staining

For immunofluorescence analyses the cells-laden hydrogel drops (both in static and dynamic experiments) cultured for 8 days were washed twice with PBS, fixed with 4% PFA, and permeabilized in 0.2% PBS/Triton X-100 for 15 min. Blocking solution (2% BSA in 0.1% PBS/Triton) was added for 1 h at room temperature. U87-MG cells were stained with CD44 antibody, while SVG-A cells were stained with GFAP AlexaFluor-488 conjugated antibody at 4°C overnight. A secondary antibody for CD44 and TRITC-Phalloidin were added to the samples for 25 min at room temperature. Cell nuclei were stained with DAPI. HIF1α staining of the microfluidic chips was performed following the same protocol described above, with the only modification that the chips were unsealed before starting the staining procedure. Fluorescent images were obtained by a Carl Zeiss confocal microscope (LSM700) using an EC Plan-Neofluar 40X/1.3 oil-immersion objective. List of antibodies, source, and concentration is reported in Table S3.

4.22. Statistical analysis

The number of performed experiments is indicated in the figure legends. For qualitative analyses, such as those obtained from immunofluorescence, images are representative of what was observed in at least three independent samples or replicates. GraphPad Prism v.10 was used for statistical analyses. Data are presented as the mean ± SD of at least three independent experiments (n = 3). Significance was calculated by analysis of variance (ANOVA) (p: <0.05 (*), <0.01 (**), <0.001 (***), <0.0001 (****), ns: not significant).

CRediT authorship contribution statement

Gaia Corallo: Formal analysis, Methodology, Writing – original draft. **Laura Sercia:** Formal analysis, Methodology, Writing – original draft. **Alessandro De Giorgi:** Formal analysis, Methodology, Writing – original draft. **Francesca Scalera:** Methodology, Writing – review & editing. **Alberto Portone:** Methodology, Writing – review & editing. **Paola Franco:** Conceptualization, Writing – review & editing. **Maria Patrizia Stoppelli:** Conceptualization, Funding acquisition, Writing – review & editing. **Giuseppe Gigli:** Funding acquisition, Project administration. **Alessandro Polini:** Conceptualization, Funding acquisition, Project administration, Writing – review & editing. **Francesca Gervaso:** Conceptualization, Funding acquisition, Project administration, Writing – review & editing.

Declaration of competing interests

The authors declare that they have no known competing financial interests or personal relationships that could have appeared to influence the work reported in this paper.

Acknowledgements

The authors acknowledge the Italian Ministry of Research (MUR) under the complementary actions to the NRRP "D34 Health" Grant (# PNC0000001) and "Fit4MedRob – Fit for Medical Robotics" Grant (#PNC0000007). The study was supported also by the "Tecnopolo per la medicina di precisione" (TecnoMed Puglia) - Regione Puglia DGR n.2117 of 21/11/2018, CUP: B84I18000540002, by the Italian Ministry of Health, FSC 2014-2020, Code T4-AN-01 (CUP: F83C22001560003) and by the "National Center for Gene Therapy and Drug based on RNA Technology", funded by the European Union - Next Generation EU-NRRP M4.C2- Investment 1.4 (CN00000041 CN3 RNA). Finally, the authors acknowledge the ZEISS labs@location partnership between ZEISS Italy and the CNR NANOTEC for providing application and technical support.

Appendix A. Supplementary data

Supplementary data to this article can be found online at https://doi.org/10.1016/j.mtbio.2026.103548.

Data availability

Data will be made available on request.

References

[1] M. Khabibov, A. Garifullin, Y. Boumber, K. Khaddour, M. Fernandez, F. Khamitov, L. Khalikova, N. Kuznetsova, O. Kit, L. Kharin, Signaling pathways and therapeutic approaches in glioblastoma multiforme, Int. J. Oncol. 60 (6) (2022) (Review).

[2] A. Czarnywojtek, M. Borowska, K. Dyrka, S. Van Gool, N. Sawicka-Gutaj, J. Moskal, J. Kościński, P. Graczyk, T. Hałas, A.M. Lewandowska, R. Czepczyński, M. Ruchała, Glioblastoma multiforme: the latest diagnostics and treatment techniques, Pharmacology 108 (5) (2023) 423–431.

[3] J.I. Erices, C. Bizama, I. Niechi, D. Uribe, A. Rosales, K. Fabres, G. Navarro-Martínez, Á. Torres, R. San Martín, J.C. Roa, C. Quezada-Monrás, Glioblastoma microenvironment and invasiveness: new insights and therapeutic targets, Int. J. Mol. Sci. 24 (8) (2023).

[4] M. Tang, J.N. Rich, S. Chen, Biomaterials and 3D bioprinting strategies to model glioblastoma and the blood-brain barrier, Adv. Mater. 33 (5) (2021) e2004776.
[5] X. Wang, Y. Sun, D.Y. Zhang, G.L. Ming, H. Song, Glioblastoma modeling with 3D organoids: progress and challenges, Oxf Open Neurosci 2 (2023) kvad008.
[6] L.R. Schaff, I.K. Mellinghoff, Glioblastoma and other primary brain malignancies in adults: a review, JAMA 329 (7) (2023) 574–587.
[7] L. Rong, N. Li, Z. Zhang, Emerging therapies for glioblastoma: current state and future directions, J. Exp. Clin. Cancer Res. 41 (1) (2022) 142.
[8] K. Petrecca, M.C. Guiot, V. Panet-Raymond, L. Souhami, Failure pattern following complete resection plus radiotherapy and temozolomide is at the resection margin in patients with glioblastoma, J. Neuro Oncol. 111 (1) (2013) 19–23.
[9] N.A. Charles, E.C. Holland, R. Gilbertson, R. Glass, H. Kettenmann, The brain tumor microenvironment, Glia 59 (8) (2011) 1169–1180.
[10] H.F. Dvorak, V.M. Weaver, T.D. Tlsty, G. Bergers, Tumor microenvironment and progression, J. Surg. Oncol. 103 (6) (2011) 468–474.
[11] P. Sharma, A. Aaroe, J. Liang, V.K. Puduvalli, Tumor microenvironment in glioblastoma: current and emerging concepts, Neuro-Oncology Advances 5 (1) (2023).
[12] B.C. Prager, Q. Xie, S. Bao, J.N. Rich, Cancer stem cells: the architects of the tumor ecosystem, Cell Stem Cell 24 (1) (2019) 41–53.
[13] M. Dapash, D. Hou, B. Castro, C. Lee-Chang, M.S. Lesniak, The interplay between glioblastoma and its microenvironment, Cells 10 (9) (2021).
[14] K.M. Stanke, S. Kidambi, Direct-contact Co-culture of astrocytes and glioblastoma cells patterned using polyelectrolyte multilayer templates, J. Vis. Exp. 184 (2022).
[15] J. White, M.P.J. White, A. Wickremesekera, L. Peng, C. Gray, The tumour microenvironment, treatment resistance and recurrence in glioblastoma, J. Transl. Med. 22 (1) (2024) 540.
[16] A. Bikfalvi, C.A. da Costa, T. Avril, J.V. Barnier, L. Bauchet, L. Brisson, P. F. Cartron, H. Castel, E. Chevet, H. Chneiweiss, A. Clavreul, B. Constantin, V. Coronas, T. Daubon, M. Dontenwill, F. Ducray, N. Enz-Werle, D. Figarella-Branger, I. Fournier, J.S. Frenel, M. Gabut, T. Galli, J. Gavard, G. Huberfeld, J. P. Hugnot, A. Idbaih, M.P. Junier, T. Mathivet, P. Menei, D. Meyronet, C. Mirjolet, F. Morin, J. Mosser, E.C. Moyal, V. Rousseau, M. Salzet, M. Sanson, G. Seano, E. Tabouret, A. Tchoghandjian, L. Turchi, F.M. Vallette, S. Vats, M. Verreault, T. Virolle, Challenges in glioblastoma research: focus on the tumor microenvironment, Trends Cancer 9 (1) (2023) 9–27.
[17] T. Stanković, T. Ranđelović, M. Dragoj, S.S. Burić, L. Fernández, I. Ochoa, V. M. Pérez-García, M. Pešić, In vitro biomimetic models for glioblastoma-a promising tool for drug response studies, Drug Resist. Updates 55 (2021) 100753.
[18] N.A. Khiabani, M.A. Doustvandi, D. Story, S.A. Nobari, M. Hajizadeh, R. Petersen, G. Dunbar, J. Rossignol, Glioblastoma therapy: state of the field and future prospects, Life Sci. 359 (2024) 123227.
[19] H. Jo, S. Lee, M.H. Kim, S. Park, S.Y. Lee, Recapitulating glioma stem cell niches using 3D spheroid models for glioblastoma research, Biosensors (Basel) 14 (11) (2024).
[20] M. Paolillo, S. Comincini, S. Schinelli, In vitro glioblastoma models: a journey into the third dimension, Cancers (Basel) 13 (10) (2021).
[21] N. Yadav, B.W. Purow, Understanding current experimental models of glioblastoma-brain microenvironment interactions, J. Neuro Oncol. 166 (2) (2024) 213–229.
[22] F.C. Chang, S.L. Levengood, N. Cho, L. Chen, E. Wang, J.S. Yu, M. Zhang, Crosslinked Chitosan-PEG hydrogel for culture of human glioblastoma cell spheroids and drug screening, Adv. Ther. 1 (7) (2018).
[23] A.E. Erickson, S.K. Lan Levengood, J. Sun, F.C. Chang, M. Zhang, Fabrication and characterization of chitosan-hyaluronic acid scaffolds with varying stiffness for glioblastoma cell culture, Adv. Healthcare Mater. 7 (15) (2018) e1800295.
[24] G. Morello, G. De Iaco, G. Gigli, A. Polini, F. Gervaso, Chitosan and pectin hydrogels for tissue engineering and in vitro modeling, Gels 9 (2) (2023).
[25] J.L. King, P. Maturavongsadit, S.D. Hingtgen, S.R. Benhabbour, Injectable pH thermo-responsive hydrogel scaffold for tumoricidal neural stem cell therapy for glioblastoma multiforme, Pharmaceutics 14 (10) (2022).
[26] S.H. Aswathy, U. Narendrakumar, I. Manjubala, Commercial hydrogels for biomedical applications, Heliyon 6 (4) (2020) e03719.
[27] S.R. Caliari, J.A. Burdick, A practical guide to hydrogels for cell culture, Nat. Methods 13 (5) (2016) 405–414.
[28] P. Erkoc, F. Seker, T. Bagci-Onder, S. Kizilel, Gelatin methacryloyl hydrogels in the absence of a crosslinker as 3D glioblastoma multiforme (GBM)-mimetic microenvironment, Macromol. Biosci. 18 (3) (2018).
[29] K.Y. Amofa, K.M. Patterson, J. Ortiz, S. Kumar, Dissecting TGF-β-induced glioblastoma invasion with engineered hyaluronic acid hydrogels, APL Bioeng. 8 (2) (2024) 026125.
[30] Y. Kim, S. Kumar, CD44-mediated adhesion to hyaluronic acid contributes to mechanosensing and invasive motility, Mol. Cancer Res. 12 (10) (2014) 1416–1429.
[31] S. Pedron, G.L. Wolter, J.E. Chen, S.E. Laken, J.N. Sarkaria, B.A.C. Harley, Hyaluronic acid-functionalized gelatin hydrogels reveal extracellular matrix signals temper the efficacy of erlotinib against patient-derived glioblastoma specimens, Biomaterials 219 (2019) 119371.
[32] G. Safarians, A. Sohrabi, I. Solomon, W. Xiao, S. Bastola, B.W. Rajput, M. Epperson, I. Rosenzweig, K. Tamura, B. Singer, J. Huang, M.J. Harrison, T. Sanazzaro, M.C. Condro, H.I. Kornblum, S.K. Seidlits, Glioblastoma spheroid invasion through soft, brain-like matrices depends on hyaluronic Acid-CD44 interactions, Adv. Healthcare Mater. 12 (14) (2023) e2203143.
[33] W. Xiao, A. Ehsanipour, A. Sohrabi, S.K. Seidlits, Hyaluronic-acid based hydrogels for 3-Dimensional culture of patient-derived glioblastoma cells, J. Vis. Exp. 138 (2018).
[34] A. Acharekar, K. Bachal, P. Shirke, R. Thorat, A. Banerjee, N. Gardi, A. Majumder, S. Dutt, Substrate stiffness regulates the recurrent glioblastoma cell morphology and aggressiveness, Matrix Biol. 115 (2023) 107–127.
[35] K. Wang, F.M. Kievit, A.E. Erickson, J.R. Silber, R.G. Ellenbogen, M. Zhang, Culture on 3D chitosan-hyaluronic acid scaffolds enhances stem cell marker expression and drug resistance in human glioblastoma cancer stem cells, Adv. Healthcare Mater. 5 (24) (2016) 3173–3181.
[36] V.A. Kriuchkovskaia, E.K. Eames, R.B. Riggins, B.A.C. Harley, Acquired temozolomide resistance instructs patterns of glioblastoma behavior in gelatin hydrogels, Adv. Healthcare Mater. 13 (27) (2024) e2400779.
[37] L. Liang, R. Cui, S. Zhong, Z. Wang, Z. He, H. Duan, X. Guo, J. Lu, H. Hu, C. Li, C. Yu, Y. Yu, C. Guo, Y. Mou, Analysis of the potential role of photocurable hydrogel in patient-derived glioblastoma organoid culture through RNA sequencing, Biomater. Sci. 10 (17) (2022) 4902–4914.
[38] M.T. Ngo, B.A.C. Harley, Perivascular signals alter global gene expression profile of glioblastoma and response to temozolomide in a gelatin hydrogel, Biomaterials 198 (2019) 122–134.
[39] S. Pedron, J.S. Hanselman, M.A. Schroeder, J.N. Sarkaria, B.A.C. Harley, Extracellular hyaluronic acid influences the efficacy of EGFR tyrosine kinase inhibitors in a biomaterial model of glioblastoma, Adv. Healthcare Mater. 6 (21) (2017).
[40] N. Shah, P.M. Hallur, R.A. Ganesh, P. Sonpatki, D. Naik, K.P. Chandrachari, R. B. Puchalski, A. Chaubey, Gelatin methacrylate hydrogels culture model for glioblastoma cells enriches for mesenchymal-like state and models interactions with immune cells, Sci. Rep. 11 (1) (2021) 17727.
[41] A. Stanzione, A. Polini, F. Scalera, G. Gigli, L. Moroni, F. Gervaso, Photo/thermo-sensitive chitosan and gelatin-based interpenetrating polymer network for mimicking muscle tissue extracellular matrix, Heliyon 10 (21) (2024) e39820.
[42] G. Akcay, R. Luttge, Stiff-to-Soft transition from glass to 3D hydrogel substrates in neuronal cell culture, Micromachines 12 (2) (2021).
[43] K. Yue, G. Trujillo-de Santiago, M.M. Alvarez, A. Tamayol, N. Annabi, A. Khademhosseini, Synthesis, properties, and biomedical applications of gelatin methacryloyl (GelMA) hydrogels, Biomaterials 73 (2015) 254–271.
[44] F. Bisconti, B. Vilardo, G. Corallo, F. Scalera, G. Gigli, A. Chiocchetti, A. Polini, F. Gervaso, An assist for arthritis studies: a 3D cell culture of human fibroblast-like synoviocytes by encapsulation in a chitosan-based hydrogel, Adv. Therapeut. 7 (12) (2024) 2400166.
[45] R. Rizzo, V. Onesto, G. Morello, H. Iuele, F. Scalera, S. Forciniti, G. Gigli, A. Polini, F. Gervaso, L.L. Del Mercato, pH-sensing hybrid hydrogels for non-invasive metabolism monitoring in tumor spheroids, Mater. Today Bio 20 (2023) 100655.
[46] N.H. Do, Q.T. Truong, P.K. Le, A.C. Ha, Recent developments in chitosan hydrogels carrying natural bioactive compounds, Carbohydr. Polym. 294 (2022) 119726.
[47] M.C. Pellá, M.K. Lima-Tenório, E.T. Tenório-Neto, M.R. Guilherme, E.C. Muniz, A. F. Rubira, Chitosan-based hydrogels: from preparation to biomedical applications, Carbohydr. Polym. 196 (2018) 233–245.
[48] A. Stanzione, A. Polini, V. La Pesa, A. Quattrini, A. Romano, G. Gigli, L. Moroni, F. Gervaso, Thermosensitive chitosan-based hydrogels supporting motor neuron-like NSC-34 cell differentiation, Biomater. Sci. 9 (22) (2021) 7492–7503.
[49] L. Parès, S. Naasri, L. Delattre, H. Therriault, B. Liberelle, G. De Crescenzo, M. A. Lauzon, N. Faucheux, B. Paquette, N. Virgilio, Macroporous chitosan/alginate hydrogels crosslinked with genipin accumulate and retain glioblastoma cancer cells, RSC Adv. 14 (48) (2024) 35286–35304.
[50] A. Stanzione, A. Polini, V. La Pesa, A. Romano, A. Quattrini, G. Gigli, L. Moroni, F. Gervaso, Development of injectable thermosensitive chitosan-based hydrogels for cell encapsulation, Appl. Sci. 10 (18) (2020) 6550.
[51] P. Civita, M.L. D, G.J. Pilkington, Pre-clinical drug testing in 2D and 3D human in vitro models of glioblastoma incorporating non-neoplastic astrocytes: tunneling nano tubules and mitochondrial transfer modulates cell behavior and therapeutic response, Int. J. Mol. Sci. 20 (23) (2019).
[52] D.C. Watson, D. Bayik, S. Storevik, S.S. Moreino, S.A. Sprowls, J. Han, M. T. Augustsson, A. Lauko, P. Sravya, G.V. Røsland, K. Troike, K.J. Tronstad, S. Wang, K. Sarnow, K. Kay, T.R. Lunavat, D.J. Silver, S. Dayal, J.V. Joseph, E. Mulkearns-Hubert, L.A.R. Ystaas, G. Deshpande, J. Guyon, Y. Zhou, C. R. Magaut, J. Seder, L. Neises, S.E. Williford, J. Meiser, A.J. Scott, P. Sajjakulnukit, J.A. Mears, R. Bjerkvig, A. Chakraborty, T. Daubon, F. Cheng, C. A. Lyssiotis, D.R. Wahl, A.B. Hjelmeland, J.A. Hossain, H. Miletic, J.D. Lathia, GAP43-dependent mitochondria transfer from astrocytes enhances glioblastoma tumorigenicity, Nat. Cancer 4 (5) (2023) 648–664.
[53] S. Maity, T. Bhuyan, C. Jewell, S. Kawakita, S. Sharma, H.T. Nguyen, A. Hassani Najafabadi, M. Ermis, N. Falcone, J. Chen, K. Mandal, D. Khorsandi, C. Yilgor, A. Choroomi, E. Torres, M. Mecwan, J.V. John, M. Akbari, Z. Wang, D. Moniz-Garcia, A. Quiñones-Hinojosa, V. Jucaud, M.R. Dokmeci, A. Khademhosseini, Recent developments in Glioblastoma-On-A-Chip for advanced drug screening applications, Small 21 (1) (2025) e2405511.
[54] G. Thenuwara, B. Javed, B. Singh, F. Tian, Biosensor-enhanced Organ-on-a-Chip models for investigating glioblastoma tumor microenvironment dynamics, Sensors (Basel) 24 (9) (2024).
[55] L. Yang, C. Lin, L. Wang, H. Guo, X. Wang, Hypoxia and hypoxia-inducible factors in glioblastoma multiforme progression and therapeutic implications, Exp. Cell Res. 318 (19) (2012) 2417–2426.

[56] E.E. Bar, A. Lin, V. Mahairaki, W. Matsui, C.G. Eberhart, Hypoxia increases the expression of stem-cell markers and promotes clonogenicity in glioblastoma neurospheres, Am. J. Pathol. 177 (3) (2010) 1491–1502.

[57] T. Beppu, K. Kamada, Y. Yoshida, H. Arai, K. Ogasawara, A. Ogawa, Change of oxygen pressure in glioblastoma tissue under various conditions, Journal of neuro-oncology 58 (1) (2002) 47–52.

[58] A. Carreau, B.E. Hafny-Rahbi, A. Matejuk, C. Grillon, C. Kieda, Why is the partial oxygen pressure of human tissues a crucial parameter? Small molecules and hypoxia, J. Cell Mol. Med. 15 (6) (2011) 1239–1253.

[59] M.W. Dewhirst, Y. Cao, B. Moeller, Cycling hypoxia and free radicals regulate angiogenesis and radiotherapy response, Nat. Rev. Cancer 8 (6) (2008) 425–437.

[60] Z. Li, S. Bao, Q. Wu, H. Wang, C. Eyler, S. Sathornsumetee, Q. Shi, Y. Cao, J. Lathia, R.E. McLendon, Hypoxia-inducible factors regulate tumorigenic capacity of glioma stem cells, Cancer Cell 15 (6) (2009) 501–513.

[61] J. Heddleston, Z. Li, J. Lathia, S. Bao, A. Hjelmeland, J. Rich, Hypoxia inducible factors in cancer stem cells, Br. J. Cancer 102 (5) (2010) 789–795.

[62] S. Jawhari, M.-H. Ratinaud, M. Verdier, Glioblastoma, hypoxia and autophagy: a survival-prone 'menage-a-trois', Cell Death Dis. 7 (10) (2016) e2434-e2434.

[63] A.R. Monteiro, R. Hill, G.J. Pilkington, P.A. Madureira, The role of hypoxia in glioblastoma invasion, Cells 6 (4) (2017) 45.

[64] N.J. Mabjeesh, S. Amir, Hypoxia-inducible factor (HIF) in human tumorigenesis, Histol. Histopathol. 22 (5) (2007) 559–572.

[65] G.L. Wang, B.H. Jiang, E.A. Rue, G.L. Semenza, Hypoxia-inducible factor 1 is a basic-helix-loop-helix-PAS heterodimer regulated by cellular O2 tension, Proc. Natl. Acad. Sci. U. S. A. 92 (12) (1995) 5510–5514.

[66] M. Domènech, A. Hernández, A. Plaja, E. Martínez-Balibrea, C. Balañà, Hypoxia: the cornerstone of glioblastoma, Int. J. Mol. Sci. 22 (22) (2021) 12608.

[67] D.J. Brat, Glioblastoma: biology, genetics, and behavior, American Society of Clinical Oncology Educational Book 32 (1) (2012) 102–107.

[68] J.B. Mamani, B.S. Marinho, G.N.A. Rego, M.P. Nucci, F. Alvieri, R.S.D. Santos, J. V.M. Ferreira, F.A. Oliveira, L.F. Gamarra, Magnetic hyperthermia therapy in glioblastoma tumor on-a-Chip model, Einstein (Sao Paulo) 18 (2020) eAO4954.

[69] H.K. Yoon, X. Lou, Y.-C. Chen, Y.-E. Koo Lee, E. Yoon, R. Kopelman, Nanophotosensitizers engineered to generate a tunable mix of reactive oxygen species, for optimizing photodynamic therapy, using a microfluidic device, Chem. Mater. 26 (4) (2014) 1592–1600.

[70] M. Jie, S. Mao, H. Liu, Z. He, H.-F. Li, J.-M. Lin, Evaluation of drug combination for glioblastoma based on an intestine–liver metabolic model on microchip, Analyst 142 (19) (2017) 3629–3638.

[71] S. Liu, Z. Gong, D. Zhou, V. Ayala-Nunez, T. Xu, P. Wick, Bridging the gap: how organ-on-a-chip technology facilitates the battle against glioma, Small Sci. (2025) 2500154.

[72] T. DePalma, M. Rodriguez, L. Kollin, K. Hughes, K. Jones, E. Stagner, M. Venere, A. Skardal, A microfluidic blood brain barrier model to study the influence of glioblastoma tumor cells on BBB function, Small 21 (19) (2025) 2411361.

[73] T.J.M. Manoharan, T.Y. Wang, S. Mantri, H. Alarnous, S. Mehta, K.C. Wang, M. Nikkhah, Advancing targeted drug delivery in glioblastoma multiforme through biomimetic nanomedicine using 3D tumor-on-a-chip model, Adv. Healthcare Mater. 15 (4) (2026) e02454.

[74] C. Kolliopoulos, M.M. Ali, C. Castillejo-Lopez, C.H. Heldin, P. Heldin, CD44 depletion in glioblastoma cells suppresses growth and stemness and induces senescence, Cancers (Basel) 14 (15) (2022).

[75] D. Si, F. Yin, J. Peng, G. Zhang, High expression of CD44 predicts a poor prognosis in glioblastomas, Cancer Manag. Res. 12 (2020) 769–775.

[76] Y. Wang, L. Marucci, M.E. Homer, In silico modelling of organ-on-a-chip devices: an overview, Front. Bioeng. Biotechnol. 12 (2024) 1520795.

[77] S. Stucchi, D. Colombo, R. Guizzardi, A. D'Aloia, M. Collini, M. Bouzin, B. Costa, M. Ceriani, A. Natalello, P. Pallavicini, Squarate cross-linked gelatin hydrogels as three-dimensional scaffolds for biomedical applications, Langmuir 37 (48) (2021) 14050–14058.

[78] C. Garcia-Aparicio, I. Quijada-Garrido, L. Garrido, Diffusion of small molecules in a chitosan/water gel determined by proton localized NMR spectroscopy, J. Colloid Interface Sci. 368 (1) (2012) 14–20.

[79] J. Ayensa-Jiménez, M. Pérez-Aliacar, T. Randelovic, S. Oliván, L. Fernández, J. A. Sanz-Herrera, I. Ochoa, M.H. Doweidar, M. Doblaré, Mathematical formulation and parametric analysis of in vitro cell models in microfluidic devices: application to different stages of glioblastoma evolution, Sci. Rep. 10 (1) (2020) 21193.

[80] S. Bupphathong, C. Quiroz, W. Huang, P.F. Chung, H.Y. Tao, C.H. Lin, Gelatin methacrylate hydrogel for tissue engineering Applications-A review on material modifications, Pharmaceuticals 15 (2) (2022).

[81] C. Traldi, V. Chiappini, G. Menduti, C. Tonda-Turo, M. Boido, Advanced materials and biofabrication technologies to design in vitro functional central nervous system models, Frontiers in Medical Engineering 1 (2023) 1270943.

[82] M. Dash, F. Chiellini, R.M. Ottenbrite, E. Chiellini, Chitosan—A versatile semi-synthetic polymer in biomedical applications, Prog. Polym. Sci. 36 (8) (2011) 981–1014.

[83] M. Zhou, B.H. Lee, Y.J. Tan, L.P. Tan, Microbial transglutaminase induced controlled crosslinking of gelatin methacryloyl to tailor rheological properties for 3D printing, Biofabrication 11 (2) (2019) 025011.

[84] M.D. Norman, S.A. Ferreira, G.M. Jowett, L. Bozec, E. Gentleman, Measuring the elastic modulus of soft culture surfaces and three-dimensional hydrogels using atomic force microscopy, Nat. Protoc. 16 (5) (2021) 2418–2449.

[85] L. Sercia, A. Portone, S. Leporatti, S. Belli, P. Franco, M.P. Stoppelli, G. Gigli, A. Polini, F. Gervaso, Simple fabrication method for cancer cell migration studies on biomimetic substrates with tunable stiffness, Mater. Today Bio 39 (2026) 103332.

[86] M.J. Clark, N. Homer, B.D. O'Connor, Z. Chen, A. Eskin, H. Lee, B. Merriman, S. F. Nelson, U87MG decoded: the genomic sequence of a cytogenetically aberrant human cancer cell line, PLoS Genet. 6 (1) (2010) e1000832.

[87] M. Allen, M. Bjerke, H. Edlund, S. Nelander, B. Westermark, Origin of the U87MG glioma cell line: good news and bad news, Sci. Transl. Med. 8 (354) (2016) 354re3.

[88] J.A. Schulz, L.T. Rodgers, R.J. Kryscio, A.M.S. Hartz, B. Bauer, Characterization and comparison of human glioblastoma models, BMC Cancer 22 (1) (2022) 844.

[89] X. Guan, M.N. Hasan, S. Maniar, W. Jia, D. Sun, Reactive astrocytes in glioblastoma multiforme, Mol. Neurobiol. 55 (8) (2018) 6927–6938.

[90] C. Escartin, E. Galea, A. Lakatos, J.P. O'Callaghan, G.C. Petzold, A. Serrano-Pozo, C. Steinhäuser, A. Volterra, G. Carmignoto, A. Agarwal, N.J. Allen, A. Araque, L. Barbeito, A. Barzilai, D.E. Bergles, G. Bonvento, A.M. Butt, W.T. Chen, M. Cohen-Salmon, C. Cunningham, B. Deneen, B. De Strooper, B. Díaz-Castro, C. Farina, M. Freeman, V. Gallo, J.E. Goldman, S.A. Goldman, M. Götz, A. Gutiérrez, P.G. Haydon, D.H. Heiland, E.M. Hol, M.G. Holt, M. Iino, K. V. Kastanenka, H. Kettenmann, B.S. Khakh, S. Koizumi, C.J. Lee, S.A. Liddelow, B. A. MacVicar, P. Magistretti, A. Messing, A. Mishra, A.V. Molofsky, K.K. Murai, C. M. Norris, S. Okada, S.H.R. Oliet, J.F. Oliveira, A. Panatier, V. Parpura, M. Pekna, M. Pekny, L. Pellerin, G. Perea, B.G. Pérez-Nievas, F.W. Pfrieger, K.E. Poskanzer, F.J. Quintana, R.M. Ransohoff, M. Riquelme-Perez, S. Robel, C.R. Rose, J. D. Rothstein, N. Rouach, D.H. Rowitch, A. Semyanov, S. Sirko, H. Sontheimer, R. A. Swanson, J. Vitorica, I.B. Wanner, L.B. Wood, J. Wu, B. Zheng, E.R. Zimmer, R. Zorec, M.V. Sofroniew, A. Verkhratsky, Reactive astrocyte nomenclature, definitions, and future directions, Nat. Neurosci. 24 (3) (2021) 312–325.

[91] Y. Cui, P. Lee, J.J. Reardon, A. Wang, S. Lynch, J.J. Otero, G. Sizemore, J. O. Winter, Evaluating glioblastoma tumour sphere growth and migration in interaction with astrocytes using 3D collagen-hyaluronic acid hydrogels, J. Mater. Chem. B 11 (24) (2023) 5442–5459.

[92] P.S. Nakod, Y. Kim, S.S. Rao, The impact of astrocytes and endothelial cells on glioblastoma stemness marker expression in multicellular spheroids, Cell. Mol. Bioeng. 14 (6) (2021) 639–651.

[93] P. Sivashankari, M. Prabaharan, Prospects of chitosan-based scaffolds for growth factor release in tissue engineering, Int. J. Biol. Macromol. 93 (2016) 1382–1389.

[94] A.K. Miri, H.G. Hosseinabadi, B. Cecen, S. Hassan, Y.S. Zhang, Permeability mapping of gelatin methacryloyl hydrogels, Acta Biomater. 77 (2018) 38–47.

[95] J. Sun, Y.T. Chan, K.W.K. Ho, L. Zhang, L. Bian, R.S. Tuan, Y. Jiang, "Slow walk" mimetic tensile loading maintains human meniscus tissue resident progenitor cells homeostasis in photocrosslinked gelatin hydrogel, Bioact. Mater. 25 (2023) 256–272.

[96] Y. Fan, D.T. Nguyen, Y. Akay, F. Xu, M. Akay, Engineering a brain cancer chip for high-throughput drug screening, Sci. Rep. 6 (2016) 25062.

[97] E. De Vitis, V. La Pesa, F. Gervaso, A. Romano, A. Quattrini, G. Gigli, L. Moroni, A. Polini, A microfabricated multi-compartment device for neuron and schwann cell differentiation, Sci. Rep. 11 (1) (2021) 7019.

[98] L.A. Milton, M.S. Viglione, L.J.Y. Ong, G.P. Nordin, Y.C. Toh, Vat photopolymerization 3D printed microfluidic devices for organ-on-a-chip applications, Lab Chip 23 (16) (2023) 3537–3560.

[99] A. Bucciarelli, X. Paolelli, E. De Vitis, N. Selicato, F. Gervaso, G. Gigli, L. Moroni, A. Polini, VAT photopolymerization 3D printing optimization of high aspect ratio structures for additive manufacturing of chips towards biomedical applications, Addit. Manuf. 60 (2022) 103200.

[100] V. Carvalho, N. Rodrigues, R. Ribeiro, P.F. Costa, J.C.F. Teixeira, R.A. Lima, S. Teixeira, Hemodynamic study in 3D printed stenotic coronary artery models: experimental validation and transient simulation, Comput. Methods Biomech. Biomed. Eng. 24 (6) (2021) 623–636.

[101] E. Doutel, N. Viriato, J. Carneiro, J. Campos, J.M. Miranda, Geometrical effects in the hemodynamics of stenotic and non-stenotic left coronary arteries-numerical and in vitro approaches, Int. J. Numer. Methods Biomed. Eng. 35 (8) (2019) e3207.

[102] F. Pisapia, W. Balachandran, M. Rasekh, Organ-on-a-Chip: design and simulation of various microfluidic channel geometries for the influence of fluid dynamic parameters, Appl. Sci. 12 (8) (2022) 3829.

[103] A. Przekwas, M.R. Somayaji, Computational Pharmacokinetic Modeling of organ-on-chip Devices and Microphysiological Systems, Organ-on-a-chip, 2020, pp. 311–361.

[104] J. Hoeng, D. Bovard, M.C. Peitsch, Organ-on-a-chip: Engineered Microenvironments for Safety and Efficacy Testing, Academic Press, 2019.

[105] R.J. Gilbert, H. Park, M. Rasponi, A. Redaelli, B. Gellman, K.A. Dasse, T. Thorsen, Computational and functional evaluation of a microfluidic blood flow device, ASAIO J. 53 (4) (2007) 447–455.

[106] V. Le Maout, K. Alessandri, B. Gurchenkov, H. Bertin, P. Nassoy, G. Sciumè, Role of mechanical cues and hypoxia on the growth of tumor cells in strong and weak confinement: a dual in vitro–in silico approach, Sci. Adv. 6 (13) (2020) eaaz7130.

[107] S.R. McKeown, Defining normoxia, physoxia and hypoxia in tumours—implications for treatment response, Br. J. Radiol. 87 (1035) (2014) 20130676.

[108] M.A. Acosta, X. Jiang, P.-K. Huang, K.B. Cutler, C.S. Grant, G.M. Walker, M. P. Gamcsik, A microfluidic device to study cancer metastasis under chronic and intermittent hypoxia, Biomicrofluidics 8 (5) (2014).

[109] H.-G. Yi, Y.H. Jeong, Y. Kim, Y.-J. Choi, H.E. Moon, S.H. Park, K.S. Kang, M. Bae, J. Jang, H. Youn, S.H. Paek, D.-W. Cho, A bioprinted human-glioblastoma-on-a-chip for the identification of patient-specific responses to chemoradiotherapy, Nat. Biomed. Eng. 3 (7) (2019) 509–519.

[110] Y. Ando, H.P. Ta, D.P. Yen, S.S. Lee, S. Raola, K. Shen, A microdevice platform recapitulating hypoxic tumor microenvironments, Sci. Rep. 7 (1) (2017) 15233.

[111] S. Baek, S.E. Yu, Y.H. Deng, Y.J. Lee, D.G. Lee, S. Kim, S. Yoon, H.S. Kim, J. Park, C.H. Lee, Quenching epigenetic drug resistance using antihypoxic microparticles in glioblastoma patient-derived chips, Adv. Healthcare Mater. 11 (8) (2022) 2102226.
[112] C.-H. Hsieh, W.-C. Shyu, C.-Y. Chiang, J.-W. Kuo, W.-C. Shen, R.-S. Liu, NADPH oxidase subunit 4-mediated reactive oxygen species contribute to cycling hypoxia-promoted tumor progression in glioblastoma multiforme, PLoS One 6 (9) (2011) e23945.
[113] C.-H. Hsieh, C.-H. Lee, J.-A. Liang, C.-Y. Yu, W.-C. Shyu, Cycling hypoxia increases U87 glioma cell radioresistance via ROS induced higher and long-term HIF-1 signal transduction activity, Oncol. Rep. 24 (6) (2010) 1629–1636.
[114] J. Bou-Gharios, G. Noël, H. Burckel, Preclinical and clinical advances to overcome hypoxia in glioblastoma multiforme, Cell Death Dis. 15 (7) (2024) 503.
[115] J.H. Park, H.K. Lee, Current understanding of hypoxia in glioblastoma multiforme and its response to immunotherapy, Cancers 14 (5) (2022) 1176.
[116] D.F. Quail, J.A. Joyce, The microenvironmental landscape of brain tumors, Cancer Cell 31 (3) (2017) 326–341.
[117] B. Palazzo, S. Scialla, A. Barca, L. Sercia, D. Izzo, F. Gervaso, F. Scalera, Towards complex tissues replication: Multilayer scaffold integrating biomimetic nanohydroxyapatite/chitosan composites, Bioengineering 11 (5) (2024) 471.
[118] F. Persano, A. Parodi, T. Pallaeva, E. Kolesova, A.A. Zamyatnin Jr., V. S. Pokrovsky, V. De Matteis, S. Leporatti, M. Cascione, Atomic force microscopy: a versatile tool in cancer research, Cancers 17 (5) (2025) 858.
[119] G.-F. Richard, Trinucleotide Repeats: Methods and Protocols, Springer, 2020.
[120] H. Bruus, Governing Equations in Microfluidics, 2014.
[121] A. d'Adamo, E. Salerno, G. Corda, C. Ongaro, B. Zardin, A. Ruffini, G. Orlandi, J. Bertacchini, D. Angeli, Experimental measurements and CFD modelling of hydroxyapatite scaffolds in perfusion bioreactors for bone regeneration, Regen. Biomater. 10 (2023) rbad002.
[122] D. Sacks, B. Baxter, B.C.V. Campbell, J.S. Carpenter, C. Cognard, D. Dippel, M. Eesa, U. Fischer, K. Hausegger, J.A. Hirsch, M. Shazam Hussain, O. Jansen, M. V. Jayaraman, A.A. Khalessi, B.W. Kluck, S. Lavine, P.M. Meyers, S. Ramee, D. A. Rüfenacht, C.M. Schirmer, D. Vorwerk, Multisociety consensus quality improvement revised consensus statement for endovascular therapy of acute ischemic stroke, Int. J. Stroke 13 (6) (2018) 612–632.
[123] J.V. Green, T. Kniazeva, M. Abedi, D.S. Sokhey, M.E. Taslim, S.K. Murthy, Effect of channel geometry on cell adhesion in microfluidic devices, Lab Chip 9 (5) (2009) 677–685.
[124] P.M. Hinderliter, K.R. Minard, G. Orr, W.B. Chrisler, B.D. Thrall, J.G. Pounds, J. G. Teeguarden, ISDD: a computational model of particle sedimentation, diffusion and target cell dosimetry for in vitro toxicity studies, Part. Fibre Toxicol. 7 (1) (2010) 36.
[125] A. De Giorgi, Z. Wang, Q. Li, A. Polini, F. Gervaso, Y.S. Zhang, Computational approaches in bioprinting processes, Nat. Rev. Bioeng. (2026) 1–22.
[126] H. Qazi, Z.-D. Shi, J.M. Tarbell, Fluid shear stress regulates the invasive potential of glioma cells via modulation of migratory activity and matrix metalloproteinase expression, PLoS One 6 (5) (2011) e20348.
[127] Y. Gao, H.J. Cho, Quantifying the trade-off between stiffness and permeability in hydrogels, Soft Matter 18 (40) (2022) 7735–7740.
[128] C. Müller, A. Loman, V. Pacheco, F. Koberling, D. Willbold, W. Richtering, J. Enderlein, Precise measurement of diffusion by multi-color dual-focus fluorescence correlation spectroscopy, EPL (Europhysics Letters) 83 (4) (2008) 46001.
[129] N.S. Bhise, V. Manoharan, S. Massa, A. Tamayol, M. Ghaderi, M. Miscuglio, Q. Lang, Y. Shrike Zhang, S.R. Shin, G. Calzone, N. Annabi, T.D. Shupe, C. E. Bishop, A. Atala, M.R. Dokmeci, A. Khademhosseini, A liver-on-a-chip platform with bioprinted hepatic spheroids, Biofabrication 8 (1) (2016) 014101.
[130] P.K. Pant, R.H. Boyd, Molecular-dynamics simulation of diffusion of small penetrants in polymers, Macromolecules 26 (4) (1993) 679–686.
[131] B. DeGraff, J. Demas, Luminescence-based oxygen sensors. Reviews in Fluorescence 2005, 2005, pp. 125–151.
[132] S.M. Mavris, L.M. Hansen, Optimization of oxygen delivery within hydrogels, J. Biomech. Eng. 143 (10) (2021) 101004.
[133] F. Weise, U. Fernekorn, J. Hampl, M. Klett, A. Schober, Analysis and comparison of oxygen consumption of HepG2 cells in a monolayer and three-dimensional high density cell culture by use of a matrigrid®, Biotechnol. Bioeng. 110 (9) (2013) 2504–2512.
[134] H. Zhang, Y. Chen, X. Liu, H. Deng, Multi-omics analyses reveal mitochondrial dysfunction contributing to temozolomide resistance in glioblastoma cells, Biomolecules 13 (9) (2023).
[135] S.P. Allen, R.S. Seehra, P.R. Heath, B.P. Hall, J. Bates, C.J. Garwood, M. M. Matuszyk, S.B. Wharton, J.E. Simpson, Transcriptomic analysis of human astrocytes in vitro reveals hypoxia-induced mitochondrial dysfunction, modulation of metabolism, and dysregulation of the immune response, Int. J. Mol. Sci. 21 (21) (2020) 8028.
[136] P. Buchwald, FEM-based oxygen consumption and cell viability models for avascular pancreatic islets, Theor. Biol. Med. Model. 6 (1) (2009) 5.
[137] J. Demol, D. Lambrechts, L. Geris, J. Schrooten, H. Van Oosterwyck, Towards a quantitative understanding of oxygen tension and cell density evolution in fibrin hydrogels, Biomaterials 32 (1) (2011) 107–118.
[138] M. Shan, D. Dai, A. Vudem, J.D. Varner, A.D. Stroock, Multi-scale computational study of the warburg effect, reverse warburg effect and glutamine addiction in solid tumors, PLoS Comput. Biol. 14 (12) (2018) e1006584.
[139] L. Hathout, B. Ellingson, W. Pope, Modeling the efficacy of the extent of surgical resection in the setting of radiation therapy for glioblastoma, Cancer Sci. 107 (8) (2016) 1110–1116.
[140] A. Martínez-González, G.F. Calvo, L.A. Pérez Romasanta, V.M. Pérez-García, Hypoxic cell waves around necrotic cores in glioblastoma: a biomathematical model and its therapeutic implications, Bull. Math. Biol. 74 (12) (2012) 2875–2896.
[141] J.M. Brown, W.R. Wilson, Exploiting tumour hypoxia in cancer treatment, Nat. Rev. Cancer 4 (6) (2004) 437–447.